iScience

Article

Targeting peptidyl-arginine deiminase 4 suppresses SARS-CoV-2 replication and modulates the inflammatory response

Graphical abstract

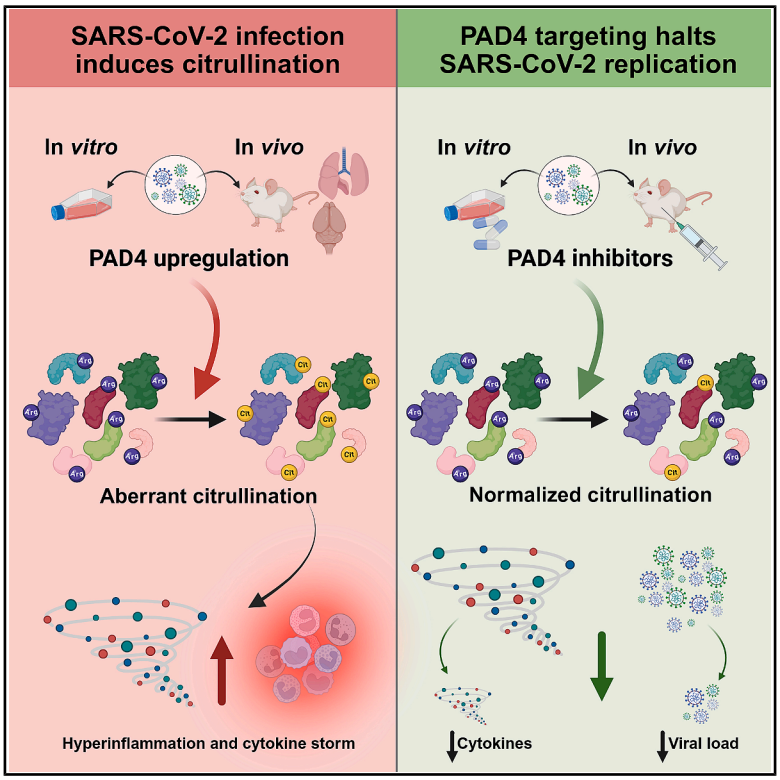

Highlights

- SARS-CoV-2 variants upregulate PAD4 in human cells and mouse lungs and brain
- 170 proteins are differentially citrullinated *in vivo* upon SARS-CoV-2 infection
- The PAD4-inhibitor GSK199 limits viral replication and inflammation *in vitro* and *in vivo*
- PAD2 is significantly downregulated in the brains of SARS-CoV-2-infected mice

Authors

Selina Pasquero, Alessandro Penna, Lucia Signorini, ..., Paul R. Thompson, Antonio Rosato, Marco De Andrea

Correspondence

marco.deandrea@unito.it

In brief

Natural sciences; Biological sciences; Microbiology; Virology

Pasquero et al., 2026, iScience *29*, 115038
March 20, 2026
https://doi.org/10.1016/j.isci.2026.115038

CellPress

iScience

CellPress
OPEN ACCESS

Article

Targeting peptidyl-arginine deiminase 4 suppresses SARS-CoV-2 replication and modulates the inflammatory response

Selina Pasquero,[1] Alessandro Penna,[2] Lucia Signorini,[3] Salvatore Villani,[4] Francesca Gugliesi,[1] Valeria Caneparo,[5] Francesco Favero,[5] Webb Camille,[6] Robert M. Green,[6] Ilaria Frasson,[7] Anna Tosi,[8] Beatrice Genova,[8] Anna Dalla Pietà,[2] Ranieri Verin,[9] Sofia Tomasoni,[9] Erika Del Grosso,[4] Serena Delbue,[3] Sara N. Richter,[7,10] Paul R. Thompson,[6] Antonio Rosato,[2,8] and Marco De Andrea[1,5,11,*]

[1]Department of Public Health and Pediatric Sciences, University of Turin - Medical School, Turin, Italy
[2]Department of Surgery, Oncology and Gastroenterology, University of Padua, Padova, Italy
[3]Department of Biomedical, Surgical and Dental Sciences, University of Milan, Milan, Italy
[4]Department of Pharmaceutical Sciences, University of Eastern Piedmont, Novara, Italy
[5]CAAD Center for Translational Research on Autoimmune and Allergic Disease, University of Eastern Piedmont, Novara Medical School, Novara, Italy
[6]Department of Biochemistry and Molecular Pharmacology, UMass Medical School, Worcester, MA, USA
[7]Department of Molecular Medicine, University of Padua, Padua, Italy
[8]Immunology and Molecular Oncology Diagnostics, Veneto Institute of Oncology IOV-IRCCS, Padua, Italy
[9]Department of Comparative Biomedicine and Food Science, University of Padua, Padua, Italy
[10]Microbiology and Virology Unit, Padua University Hospital, 35128 Padua, Italy
[11]Lead contact
*Correspondence: marco.deandrea@unito.it
https://doi.org/10.1016/j.isci.2026.115038

SUMMARY

SARS-CoV-2, the causative agent of COVID-19, remains a global concern due to gaps in understanding its pathogenesis. Peptidyl-arginine deiminases (PADs) are emerging as key regulators of viral replication and inflammation. PADs catalyze the conversion of arginine into citrulline, a modification linked to autoimmune diseases. Here, we show that PAD-mediated citrullination plays a crucial role in SARS-CoV-2 infection. Using human cell lines and in K18-hACE2 transgenic mice infected with different SARS-CoV-2 strains, we demonstrate that viral replication is associated with increased PAD4 expression. Mass spectrometry shows 170 distinct differentially citrullinated proteins in infected cells and tissues. Importantly, PAD4 inhibition significantly reduces viral replication and restores a citrullination profile comparable to that of uninfected mice. These findings suggest that SARS-CoV-2 exploits PAD-mediated citrullination to enhance replication and inflammation. Thus, targeting PAD4 may represent a viable strategy to curb viral spread and mitigate COVID-19-associated hyperinflammation.

INTRODUCTION

Since its emergence in late 2019, severe acute respiratory syndrome coronavirus 2 (SARS-CoV-2), the etiological agent of the COVID-19 pandemic, has remained a serious global threat.[1,2] Despite major advancements in our understanding of SARS-CoV-2 pathogenesis and the development of antiviral therapies[3,4] and vaccines,[5] COVID-19 still constitutes a substantial burden on public health systems globally. Indeed, between 6 January and 2 February 2025, over 147,000 new cases, 4,500 deaths, 16,700 hospitalizations, and 700 intensive care unit (ICU) admissions were reported worldwide.[6]

Besides acute infection, millions of individuals suffer from post-acute sequelae of SARS-CoV-2 infection (PASC),[7] commonly referred to as long COVID. This condition is characterized by persistent symptoms and complications affecting multiple organ systems—particularly pulmonary, cardiovascular, and neurological functions—which may persist for more than a year post-infection. However, the precise mechanisms and/or biological pathways underlying PASC are still unclear.

Although the exact pathophysiology of SARS-CoV-2 remains poorly understood, it is well established that viral replication triggers severe inflammatory responses and acute lung injury. This uncontrolled pulmonary inflammation is the major cause of COVID-19-related severity, often progressing to multiorgan failure, neurological dysfunction, and death.[1,8,9] According to the available data, the pathogenesis of COVID-19 is primarily caused by hyperproduction of pro-inflammatory cytokines such as TNF-α and IL-6, known as cytokine storm (CS), and immunothrombotic events.[10,11]

Current treatments for COVID-19 rely on two main strategies: i) suppressing inflammation through conventional

anti-inflammatory drugs (e.g., corticosteroids) and ii) inhibiting viral replication by means of direct-acting antiviral agents (DAAs).[12–14] However, recent *in vitro* and *in vivo* studies suggest that mutations in SARS-CoV-2 genome can induce resistance to approved antiviral agents,[15,16] raising concerns about the long-term efficacy of DAAs. Furthermore, the continuous emergence of SARS-CoV-2 variants capable of evading the immune system poses an ongoing challenge to vaccine effectiveness.[17,18] Thus, gaining a deeper understanding of the molecular basis of SARS-CoV-2 pathogenesis may lead to the identification of novel therapeutic targets and improve treatment strategies for COVID-19 and its long-term complications.

In recent years, post-translational modifications (PTMs) have emerged as key factors that viruses exploit to enhance their fitness during infection.[19] In this regard, a growing body of research suggests that protein citrullination plays a central role in the course of viral infections and viral pathogenesis.[20–25] This PTM, also referred to as deimination, is the hydrolysis of the guanidinium group of a peptidyl-arginine to form peptidyl-citrulline. This enzymatic conversion is catalyzed by a family of calcium-dependent enzymes known as peptidyl arginine deiminases (PADs), encoded by the *PADI* gene family (*PADI1–6*) in mammals. To date, five mammalian PAD isoenzymes have been identified, which, despite their high sequence homology, differ in tissue distribution, subcellular localization, and substrate specificity.[26,27] Consequently, these isoenzymes regulate different physiological processes, including gene expression, neural plasticity, and immune modulation.[28–30] Of note, dysregulated PAD expression and/or aberrant citrullination profiles have been implicated in several inflammatory conditions, likely contributing to autoimmune and neurodegenerative disease.[31–34]

A number of PAD inhibitors have been developed to modulate citrullination. Pan-PAD inhibitors, such as Cl-amidine (Cl-A) and BB-Cl-amidine (BB-Cl), lack isoform selectivity as they target all five PAD isozymes.[35,36] To improve specificity and reduce off-target effects, several isozyme-specific inhibitors have been synthesized in recent years, including the PAD4-specific inhibitors GSK199 and GSK484.[37,38] Both pan-PAD and PAD4-specific inhibitors have shown high therapeutic efficacy in preclinical models of inflammatory and autoimmune diseases.[37,39,40]

We have recently shown that the beta-coronavirus HCoV-OC43 heavily relies on the PAD4 isoform for replication, and that PAD4-specific inhibitors exhibit potent antiviral activity against this coronavirus in human fibroblasts.[23] Intriguingly, sera from patients with COVID-19 display elevated levels of PAD4-citrullinated histone 3 (H3),[41] a hallmark of neutrophil extracellular traps (NETs), which have been linked to thrombotic manifestations in several pathological conditions.[42] Furthermore, increased NET formation has been detected in tracheal aspirates and lung epithelial tissues of patients with COVID-19,[43] suggesting that PAD4-driven NET production may influence disease severity. Despite this evidence, the precise molecular mechanisms by which PAD4 contributes to SARS-CoV-2 pathogenesis and the characterization of the citrullinome during infection are yet to be fully elucidated.

Expanding on our previous work, we now show that *PAD4* is induced *in vitro* by different SARS-CoV-2 strains, and *in vivo* in the lungs and the brains of SARS-CoV-2-infected mice. This PAD4-specific induction is associated with a significant increase in total protein citrullination in SARS-CoV-2-infected organs compared to uninfected controls. The PAD4-specific inhibitor GSK199 consistently reduces viral particle release in the supernatant of infected Huh7.5 and Calu3 cells and suppresses viral protein production, regardless of the viral strain used. Furthermore, *in vivo* inhibition of PAD4 via intraperitoneal injection of GSK199 significantly reduces viral loads in the lungs of infected mice and the number of infectious SARS-CoV-2 particles in their nasal swabs. This antiviral effect is paralleled by a substantial decrease in pro-inflammatory gene expression in the lungs, further supporting the role of PAD4 in SARS-CoV-2-induced inflammation.

RESULTS

Severe acute respiratory syndrome coronavirus 2 infection modulates peptidyl-arginine deiminases expression *in vivo* and *in vitro*

To better understand how SARS-CoV-2 affects PAD expression, we first reanalyzed some previously published transcriptomic and proteomic raw data. Taking advantage of a COVID-19 database (http://www.biomedical-web.com/covid19db), we identified *PADI4* as the only *PAD* isoform significantly upregulated upon SARS-CoV-2 infection in a whole-blood transcriptomic study of 62 prospectively enrolled patients with COVID-19 compared to 24 healthy controls (Table S1).[44] Given that SARS-CoV-2 primarily affects the lungs, we further examined data from Wang et al.,[45] who performed genome-wide RNA sequencing (RNA-seq) on lung samples from five COVID-19 cases and four age-matched controls (Table S2). In the COVID-19 group, *PADI4*, *PADI2*, and *PADI1* genes all displayed differential expression, with *PADI4* showing the highest upregulation (Log2FC > 3).

To determine which cell types displayed higher levels of *PADI* gene expression during SARS-CoV-2 infection, we used a lung single-nucleus RNA sequencing (snRNA-seq) dataset compiled by Delorey et al.[46] This dataset included approximately 1.28 million cells and nuclei from ten studies of healthy lungs and four studies of patients with COVID-19. Each cell was categorized into one of the 28 distinct types, and two different models were used to identify genes differentially expressed between COVID-19 and healthy tissues. Our analysis revealed that *PADI4* and *PADI2* were differentially expressed in neutrophils and alveolar type 2 (AT2) cells (Figure 1A). This finding is particularly relevant as AT2 cells are the primary replication site for SARS-CoV-2. In addition, while PAD enzyme expression is well known to be altered in neutrophils during inflammatory responses, its upregulation in AT2 cells has never been reported. This suggests that, unlike the inflammation-driven regulation seen in neutrophils, the overexpression of *PADI* genes in AT2 cells may be directly triggered by SARS-CoV-2 replication itself.

To determine whether viral replication of different SARS-CoV-2 strains modulates *PAD4* and *PAD2* expression in infected human cell lines, total RNA was collected from 2020B.1-, Delta-, or Omicron-infected Calu3 and Huh7.5 cells and analyzed using qRT-PCR. As shown in Figures 1B and 1C, Delta-infected Calu3 exhibited significantly higher levels of

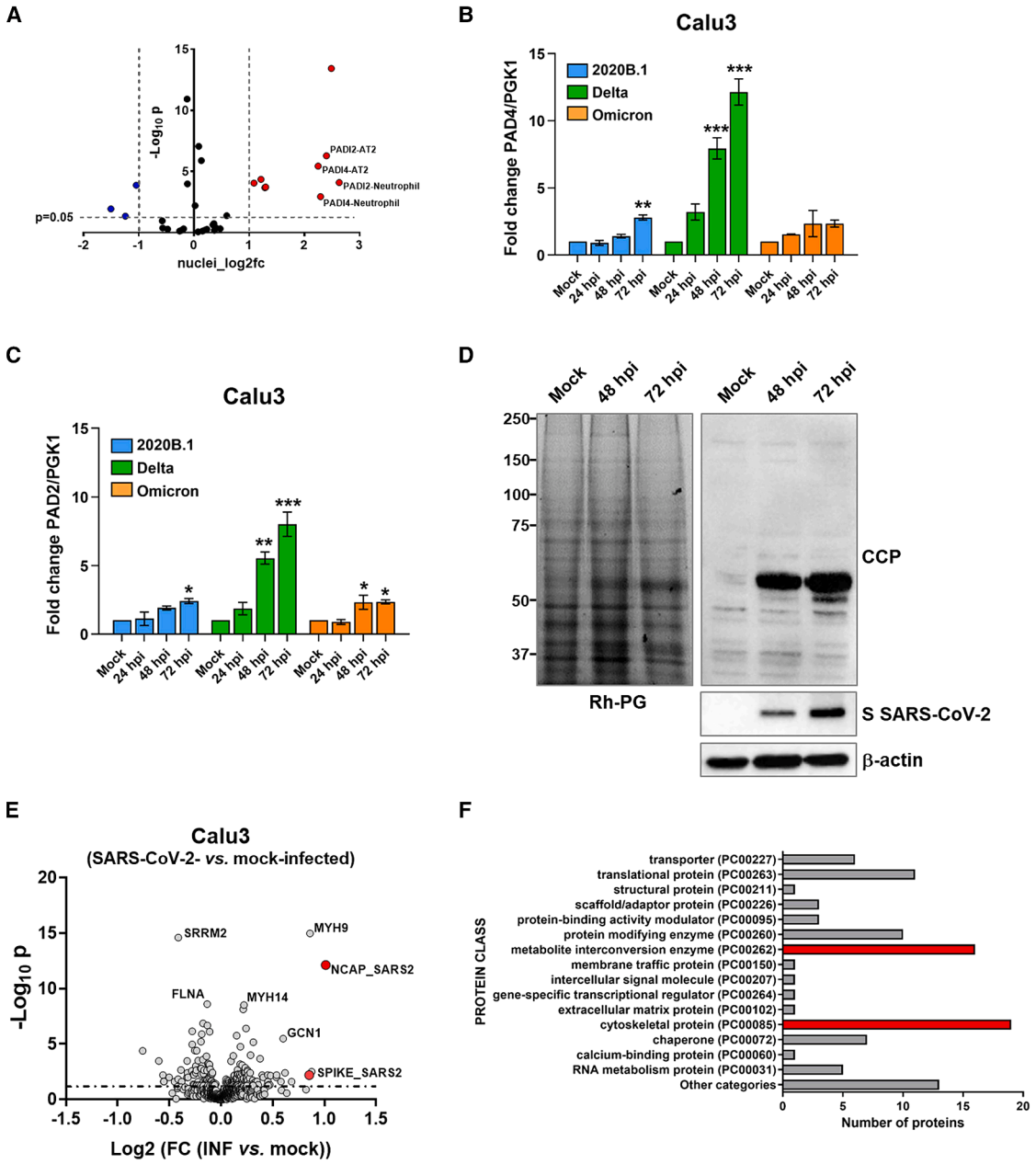

Figure 1. PAD expression *in vivo* and *in vitro* after SARS-CoV-2 infection

(A) Volcano plot relative to the reanalysis of transcriptomic data from ten studies of healthy lungs and four studies of patients with COVID-19 (Delorey et al.).

(B and C) Calu3 cells are infected with 2020B.1 (MOI 0.01), Delta (MOI 0.01), or Omicron (MOI 0.01) SARS-CoV-2 variants, and PAD4 (B) and PAD2 (C) mRNA are assessed by RT-qPCR. Data are normalized to the housekeeping gene PGK1 and expressed as mean fold change ±SEM over mock-infected cells of three independent experiments. *$p < 0.05$, **$p < 0.01$, and ***$p < 0.001$; one-way ANOVA followed by Bonferroni's post-test.

(D) Protein lysates from Calu3 infected with SARS-CoV-2 (2020B.1 variant, MOI 0.1 PFU/cell) or uninfected cells (mock) at different hours post-infection (hpi) are analyzed for citrullinated proteins using an Rh-PG citrulline-specific probe (left panel) or an anti-CCP antibody (right panel). Samples are subjected to gel electrophoresis, and SARS-CoV-2 infection is confirmed using an anti-SARS-CoV-2 Spike (S SARS-CoV-2) antibody. β-actin is used as a loading control. One representative blot of three independent experiments is shown.

(E) Volcano plot depicts host (gray dots) and viral (red dots) citrullinated proteins of SARS-infected vs. mock-infected cells at 48 hpi (2020B.1 variant, MOI 0.1 PFU/cell). The x axis represents the ratio of citrullination between mock and infected cells at the indicated time points, while the y axis indicates the statistical significance. Both variables are plotted on a logarithmic scale ($n = 3$).

(F) PANTHER classification of over-citrullinated cellular proteins based on protein classes.

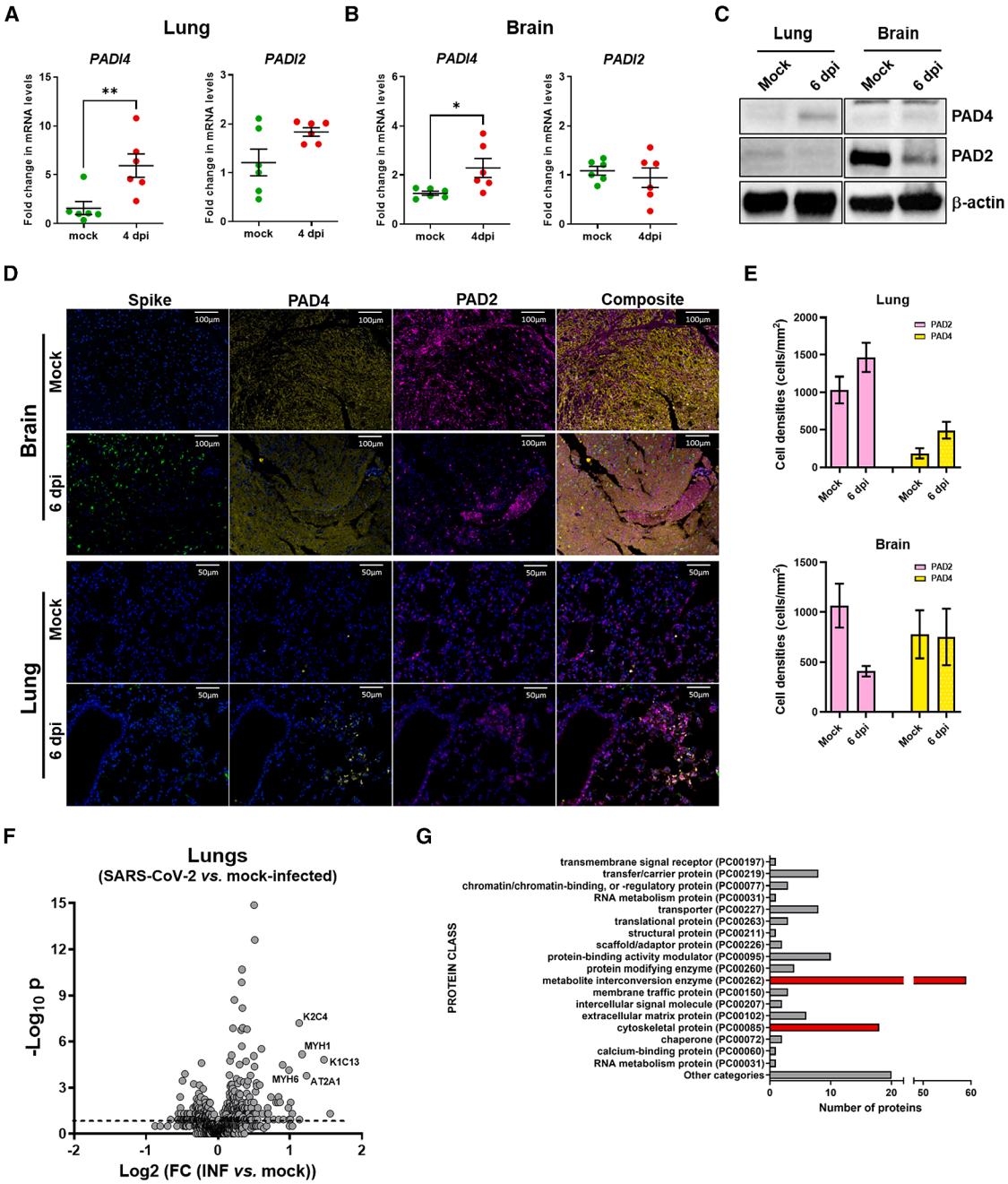

Figure 2. SARS-CoV-2 infection affects protein citrullination by modulating PAD expression *in vivo*

(A and B) PAD4 and PAD2 mRNA expression in mouse lungs (A) and brains (B) assessed by RT-qPCR. Each dot represents an individual mouse sample ($n = 6$). Data are normalized to the housekeeping gene β-actin and presented relative to one randomly selected non-infected sample. Data represent mean ± SEM. Statistical significance is determined using non parametric *t* test, $^{*}p < 0.05$.

(C) Western blot analysis of protein lysates from pooled uninfected (mock) and SARS-CoV-2-infected (6 dpi, Delta variant) mouse lungs and brains. The analysis is performed using antibodies against PAD2, PAD4, and β-actin, the latter to ensure equal loading. A representative blot from three independent experiments is shown.

(D) Multiplex immunofluorescence staining for the detection of SARS-CoV-2-targeted cells in mouse brains and lung sections at 6 dpi and mock control. S SARS-CoV-2 protein, PAD2, and PAD4 positive signals are represented in green, pink, and yellow, respectively. Cell nuclei are visualized by DAPI (blue). Original magnification 20×.

(E) Quantification of PAD2-and PAD4-positive cells is performed using the inForm Image Analysis software (Akoya Biosciences). For each mouse ($n = 6$), one representative section is analyzed to determine cell density (cells/mm^2). Data represent mean ± SEM. Statistical significance is determined using non parametric *t* test, $^{*}p < 0.05$.

(legend continued on next page)

PAD4 and *PAD2* mRNA than mock-infected controls starting at 24 hpi. While 2020B.1 and Omicron strains also induced significant *PAD4* expression, their effect were observed only at later time points and at lower levels, with approximately 3-fold upregulation compared to a 12-fold increase of Delta at 72 hpi. In Huh7.5 cells, Delta and Omicron strains significantly upregulated *PAD4* expression at 48–72 hpi (about 3-fold increase) (Figure S1A), whereas *PAD2* expression was practically left unchanged (Figure S1B). In the same experiment, 2020B.1 infection led to a significant upregulation of *PAD4* (3-folds) only at 72 h, while *PAD2* was minimally affected (Figures S1A and S1B). Consistent with *PAD4* upregulation, electrophoresis analysis of protein lysates from Calu3 infected with SARS-CoV-2 (2020B.1 strain, MOI 0.1) and incubated with the citrulline-specific probe Rh-PG showed an increase in total protein citrullination—presumably due to increased PAD enzymatic activity—compared to mock-infected cells at both 48 and 72 hpi (Figure 1D, left panel). To confirm these results, we performed immunoblot analysis on the same protein extracts using an anti-CCP antibody, which selectively recognizes citrullinated proteins. At either time point post-infection, this antibody predominantly detected proteins with molecular weights corresponding to those observed in the Rh-PG assay (Figure 1D, right panel). As expected, only SARS-CoV-2-infected cells expressed the viral spike protein (S SARS-CoV-2), confirming successful infection. A similar pattern of citrullination was observed in Huh7.5 cells infected with the SARS-CoV-2 2020B.1, Delta, or Omicron variants, as detected by both Rh-PG and anti-CCP methods (Figures S1C–S1E).

Lastly, to identify which proteins were citrullinated during infection, we employed a biotinylated citrulline-specific probe (biotin-PG) to enrich the SARS-CoV-2-associated citrullinome in Calu-3 cells using streptavidin-agarose beads (Figure 1E). We found over 700 citrullinated proteins, of which 177 were differentially citrullinated in SARS-CoV-2-infected cells vs. uninfected controls. The over-citrullinated proteins spanned multiple functional classes, including RNA metabolism proteins, calcium-binding proteins, chaperones, protein-modifying enzymes, translational proteins, and transporters (Figure 1F). However, cytoskeletal proteins and metabolite interconversion enzymes were the most represented categories. Intriguingly, two viral proteins, the nucleoprotein (N) and the spike protein (S), were also found to be citrullinated (Figure 1E, red dots).

Severe acute respiratory syndrome coronavirus 2 infection affects protein citrullination by modulating peptidyl-arginine deiminases expression *in vivo*

To experimentally validate these findings *in vivo*, K18-hACE2 transgenic mice were infected with the SARS-CoV-2 Delta strain or mock-infected to assess PAD expression and protein citrullination upon infection. Animals were monitored daily for body weight loss (Figure S2A) and clinical score (Figure S2B; Table S3). A subset of infected mice (n = 6) was euthanized at 4 dpi, a time point corresponding to the expected peak of viral replication and induction of host response factors.[47] The remaining animals were followed until the onset of severe disease and euthanized at 6 dpi, when they reached the humane endpoint, representing an advanced pathological stage. As shown in Figure 2A, *PAD4* mRNA levels were significantly upregulated in the lungs of infected mice at 4 dpi compared to mock-infected controls, with approximately a 4-fold increase, whereas *PAD2* expression was only minimally affected. Similarly, *PAD4* mRNA levels were significantly elevated in brain tissues of SARS-CoV-2-infected mice, albeit to a lesser extent than in the lungs (about 2-fold upregulation), while *PAD2* expression remained unchanged (Figure 2B). Interestingly, the brains of three SARS-CoV-2-infected mice—which also displayed the highest levels of *PAD4* expression—showed lower *PAD2* levels compared to mock-infected animals.

To further assess PAD expression at the protein level, pooled lung and brain tissues from SARS-CoV-2-infected on PAD protein expression from tissues (n = 6) and mock-infected (n = 4) mice, were analyzed at 6 dpi. Consistent with the transcriptomic results, PAD4 protein levels were increased in the lungs of infected mice (Figures 2C and S2C). PAD2 expression was barely detectable in the lungs of both SARS-CoV-2-infected and mock-infected mice but was substantially expressed in the brains of uninfected animals, consistent with its known presence in the central nervous system.[48] Surprisingly, SARS-CoV-2 infection led to a dramatic reduction in PAD2 expression in the brain (Figures 2C and S2C).

To validate these observations, we next assessed the cellular localization and expression of PAD2 and PAD4 isozymes in samples from formalin-fixed paraffin-embedded (FFPE) tissue sections from various organs of SARS-CoV-2-infected mice using specific murine antibodies. We detected PAD4 expression in neutrophils and macrophages in both the brain and lungs, with higher abundance in infected tissues (Figures S3A and S3B). Furthermore, immunofluorescence analysis revealed increased PAD4 staining in spike-positive lung areas compared to mock-infected, spike-negative tissues (Figures 2D and 2E). PAD2 staining in the lungs appeared sporadic, as reported in the literature, and no significant differences were detected between spike-positive and mock samples (Figures 2D and 2E). In contrast, in brain sections, regions containing large clusters of spike-positive cells consistently displayed a marked reduction in PAD2 staining compared with both surrounding uninfected areas and mock brains (Figures 2D and 2E).

To identify proteins undergoing citrullination *in vivo* during the symptomatic phase of infection, we used the biotin-PG probe to enrich the SARS-CoV-2-associated citrullinome in mouse lungs harvested at 6 dpi, followed by streptavidin-agarose bead isolation. We observed a dramatic change in overall protein citrullination in SARS-CoV-2-infected organs compared to

(F) Volcano plot shows citrullinated proteins in pooled protein lysates from SARS-CoV-2-infected vs. mock-infected mouse lungs at 6 dpi. Lysates are incubated with biotin-PG to isolate citrullinated proteins on streptavidin agarose, followed by on-bead tryptic digestion and LC-MS/MS analysis. Each dot represents an identified citrullinated protein. The x axis shows the citrullination ratio between mock and infected samples, and the y axis indicates statistical significance, both on a logarithmic scale (n = 3).

(G) PANTHER classification of over-citrullinated cellular proteins based on protein classes.

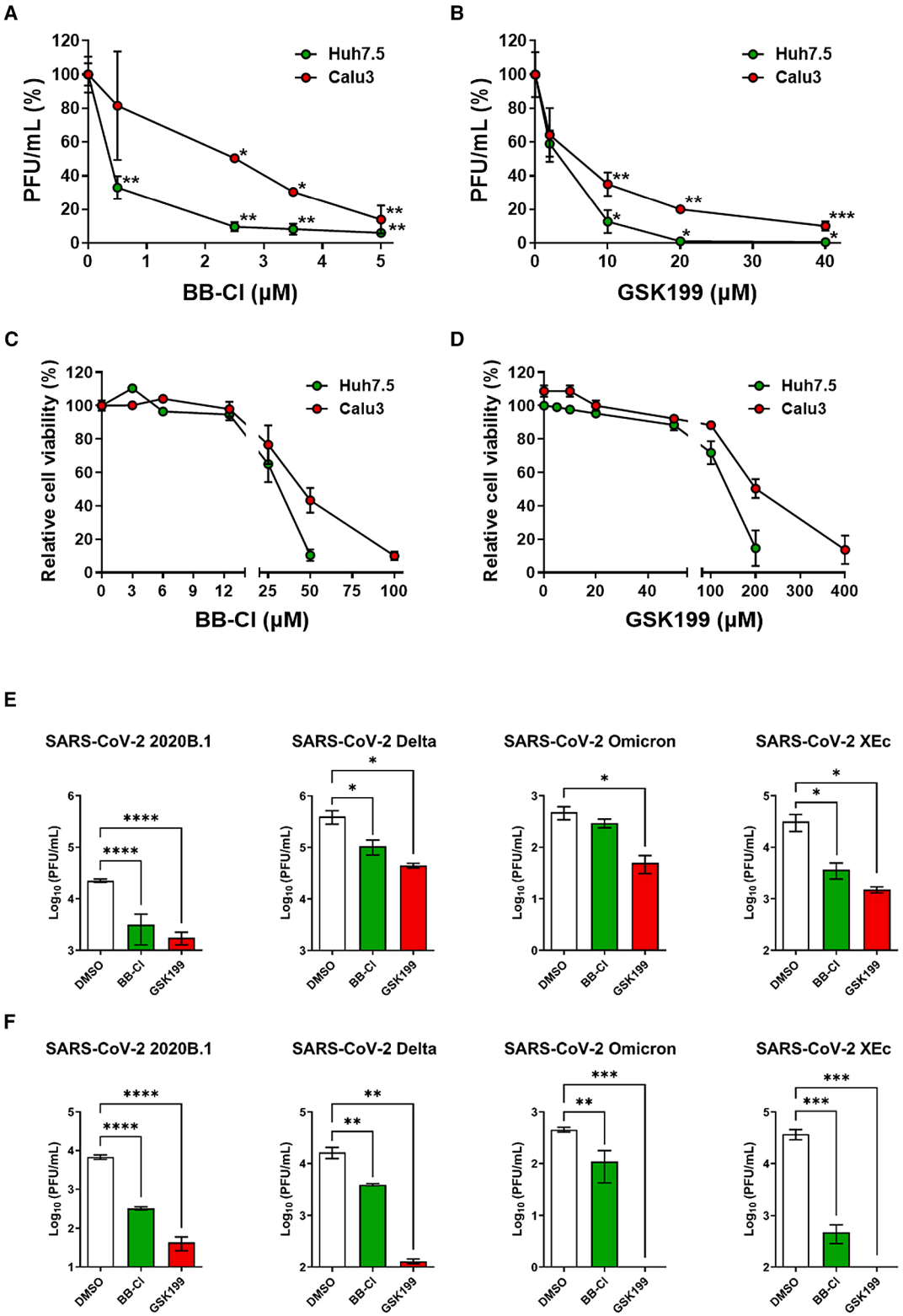

Figure 3. Antiviral effects of PAD inhibitors against SARS-CoV-2 *in vitro*

(A and B) Quantification of SARS-CoV-2 2020B.1 (MOI 0.1) viral particle production in Calu-3 and Huh7.5 cells (at 24 hpi and 48 hpi, respectively) treated with the increasing concentrations of BB-Cl (A) or GSK199 (B), determined by plaque assay. Results are expressed as a percentage relative to vehicle-treated cells

(legend continued on next page)

Table 1. CC_{50}, EC_{50}, and SI value

	CC_{50} (μM)	EC_{50} (μM)	SI
Huh7.5			
BB-Cl	25	0.25	100
GSK199	155	5.7	27
Calu3			
BB-Cl	45	2.5	18
GSK199	225	9.0	25

uninfected controls (Figure 2F), with over 200 differentially citrullinated proteins. The most represented protein classes in the over-citrullinated proteins included cytoskeletal proteins and metabolite interconversion enzymes (Figure 2G), consistent with our findings in Calu-3 cells. Additional classes included transfer/carrier proteins, chromatin/chromatin-binding proteins, transmembrane signal receptors, and protein-binding activity modulators. Notably, the most over-citrullinated proteins were cytoskeletal proteins from the myosin family (e.g., MYD1 and MYD6) and the calcium channel complex AT2A1 (Figure 2F), which is an essential regulator of cytoplasmic calcium homeostasis.[49]

Collectively, our findings indicate that SARS-CoV-2 specifically induces the transcriptional activation of PAD4 in both human and murine models. Moreover, this viral infection is also associated with specific PAD2 inhibition, at least in brain mouse tissues.

Peptidyl-arginine deiminases inhibitors block severe acute respiratory syndrome coronavirus 2 replication in human cells

To evaluate whether the enzymatic activity of PADs, particularly PAD4, played a functional role in SARS-CoV-2 replication, and whether these findings could constitute the rationale for the development of innovative antiviral drugs, we treated infected cells with different PAD inhibitors and assessed viral plaque formation. Calu3 and Huh7.5 cells were infected with the SARS-CoV-2 2020B.1 strain and treated from 1 h before infection with increasing concentrations of a pan-PAD (BB-Cl 0.6–5 μM) or PAD4-specific (GSK199, 0.25–40 μM) inhibitor. In both cell lines, continuous exposure to both PAD inhibitors resulted in a dose-dependent decrease in the amount of SARS-CoV-2 infectious viral particles compared to vehicle-treated controls (Figures 3A and 3B). The half-maximal effective concentration 50 (EC_{50}) of each inhibitor in the two cell lines was calculated and reported in Table 1.

To assess potential cytotoxic effects, we next performed a 3-(4,5-dimethylthiazol-2-yl)-2,5-diphenyl tetrazolium bromide (MTT) assay in cells treated under the same conditions and found that the inhibitors were not cytotoxic at the tested concentrations (Figures 3C and 3D). Importantly, as shown in Table 1, based on the calculated EC_{50} and the half-maximal cytotoxic concentration (CC_{50}), the selectivity indexes (SIs) of the inhibitors in SARS-CoV-2-infected Calu3 and Huh7.5 cells were consistently greater than 10. To further substantiate these findings, we tested an additional pan-PAD inhibitor (Cl-Amidine) and a second PAD4-specific inhibitor (GSK484). Both compounds showed a strong antiviral activity at completely non-toxic concentrations (Figures S4A–S4D), confirming that PADs' enzymatic activity is functionally required for efficient SARS-CoV-2 replication.

Lastly, we sought to determine whether PAD inhibition would impair the replication of additional SARS-CoV-2 variants of concern (VOCs), Delta, Omicron, and the more recent strain XEc. 2020B.1 and VOC-infected Calu3 and Huh7.5 cells were treated with BB-Cl and GSK199 at the lowest non-toxic concentrations that reduced SARS-CoV-2 2020B.1 replication by at least 90% (5 μM and 20 μM, respectively). As shown, the PAD4-specific inhibitor GSK199 was consistently effective in reducing viral particle production across all tested variants (Figures 3E and 3F), while BB-Cl displayed a milder inhibitory effect. Of note, although the Delta variant induced the strongest upregulation of PAD expression (Figures 1B and 1C), GSK199 showed a comparable antiviral efficacy also against the other strains—approximately one log reduction in Calu3 and more than two logs in Huh7.5 cells (Figures 3E and 3F). Notably, the stronger inhibitory effect observed in Huh7.5 compared to Calu3 cells may reflect their lower intrinsic capacity to sustain viral replication,[50] making them more sensitive to the additional impairment of host factors such as PAD4.

Overall, these findings indicate that PAD4 activity plays an important role in SARS-CoV-2 replication regardless of the viral strain or cell model used, and suggest that PAD4 may represent a suitable target for coronavirus therapy.

Peptidyl-arginine deiminases 4 inhibition reduces viral genome and protein synthesis after viral entry

Having established that PAD4 was the most significantly affected PAD family member in the production of new SARS-CoV-2 viral particles, we next investigated which stage of the SARS-CoV-2 life cycle PAD inhibitors could target. To this end, we performed qRT-PCR to quantify SARS-CoV-2 intracellular genome levels in Calu3 and Huh7.5 cells treated with BB-Cl or GSK199 (5 μM and 20 μM, respectively) starting 1 h before

(DMSO, marked as 0 on the graph). Data are presented as means ± SEM from four independent experiments and are analyzed by one-way ANOVA followed by Bonferroni's post-test. *$p < 0.05$, **$p < 0.01$, and ***$p < 0.001$.

(C and D) Cell viability of uninfected Calu3 and Huh7.5 cells treated with the indicated concentrations of BB-Cl (C) and GSK199 (D) for 72 h, determined for each concentration by MTT assay. Values are expressed as means ± SEM of three independent experiments.

(E) Viral titers of different SARS-CoV-2 variants are measured in Calu-3 cells at 24 hpi (MOI = 0.1) following treatment with BB-Cl (5 μM) or GSK199 (20 μM). Viral particle production is determined by plaque assay. Data are expressed as mean ± SEM from four independent experiments and analyzed by *t* test. *$p < 0.05$, **$p < 0.01$, and ***$p < 0.001$.

(F) Viral titers of different SARS-CoV-2 variants (as indicated in the figure) are measured in Huh7.5 cells at 48 hpi (MOI = 0.1) following treatment with BB-Cl (5 μM) or GSK199 (20 μM). Viral particle production is determined by plaque assay. Data are expressed as mean ± SEM from four independent experiments and analyzed by *t* test. *$p < 0.05$, **$p < 0.01$, and ***$p < 0.001$.

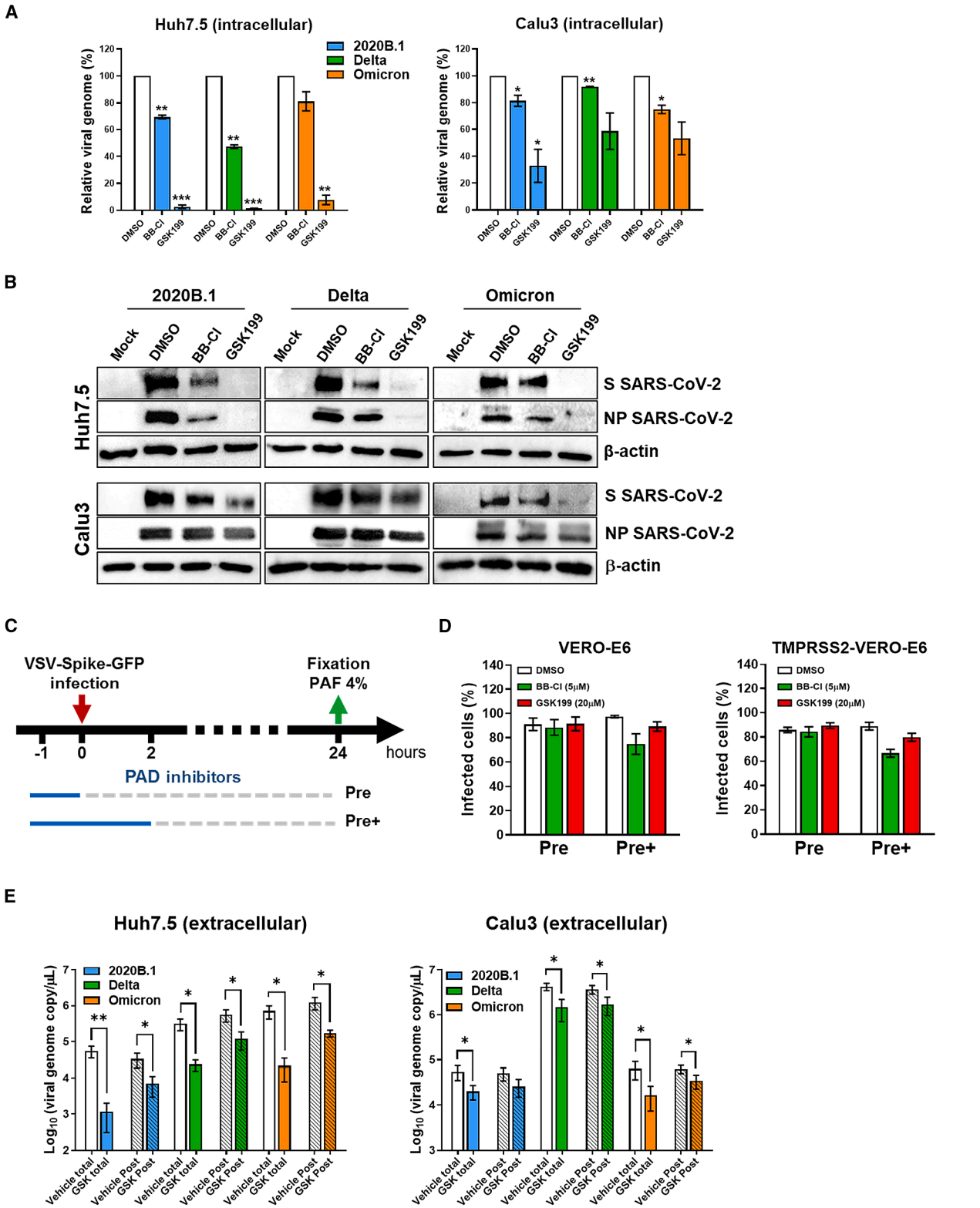

(legend on next page)

infection and infected for 24 h with 2020B.1, Delta, or Omicron strain. GSK199 consistently reduced viral genome replication across all strains and cell lines (Figure 4A). The reduction was most pronounced in Huh7.5 cells, where viral RNA levels dropped by 90% compared to mock-treated cells, whereas a significant but less substantial decrease was observed in Calu3 cells. BB-Cl treatment followed the same pattern but was generally less effective, especially in Calu3 cells. Consistent with these findings, immunoblot analysis of total protein extracts from the same experiments revealed that treatment with GSK199 led to a complete suppression of SARS-CoV-2 Spike and nucleoprotein (NP SARS-CoV-2) protein expression levels in Huh7.5 cells, while BB-Cl treatment caused a substantial—but not total—downregulation of these viral proteins compared to vehicle-treated infected cells (Figures 4B, S5A, and S5B). In contrast, in Calu3 cells, treatment with the PAD4-specific inhibitor resulted in only a moderate decrease in viral protein levels, whereas BB-Cl showed minimal effectiveness against all tested viral strains (Figures 4B, S5A, and S5B).

Since SARS-CoV-2 employs two different entry mechanisms in Huh7.5 and Calu3 cells—a pH-dependent pathway in the former and a pH-independent one in the latter[51]—we sought to determine whether the differences in inhibition efficiency observed between the two cell lines could be attributed to a differential role of PAD4 enzymatic activity in these entry routes. Thus, VSV pseudovirus assays were employed to rule out potential off-target effects of PAD inhibitors on viral attachment or entry, thereby confirming that their antiviral activity depends on the inhibition of intracellular PAD-mediated processes. To test this hypothesis, we first assessed the ability of GSK199 to limit viral entry using a replication-competent vesicular stomatitis virus-based model—namely, rVSV-eGFP-SARS-CoV-2-$_{S\Delta2}$[52]—in two cellular models representative of the two entry routes: naive VERO-E6 (pH-dependent) and TMPRSS2-expressing VERO-E6 (pH-independent). GSK199 (20 μM) and BB-Cl (5 μM) were evaluated under two treatment conditions (Figure 4C): drugs were added 1 h before infection and either washed away prior to viral addition (pre-treatment, Pre) or removed at 2 hpi (pre-treatment + infection, Pre$^+$). In both VERO-E6-based systems, GSK199 treatment did not alter the number of GFP-positive cells under either treatment protocol (Figure 4D). In contrast, exposure to BB-Cl slightly reduced the number of GFP-positive cells under the Pre$^+$ condition, suggesting an off-target effect that may inhibit viral entry.

To quantify the impact of PAD4 inhibition on SARS-CoV-2 replication, we evaluated the effect of GSK199 when added post-entry (2 hpi) and maintained throughout infection (post-treatment, Post). Regardless of the viral strain, GSK199 significantly reduced the viral load in supernatants compared to DMSO-treated controls (Figure 4E).

Overall, these findings demonstrate that PAD4 inhibition does not interfere with SARS-CoV-2 entry but effectively impairs viral genome replication and protein synthesis post-entry.

The peptidyl-arginine deiminases 4 inhibitor GSK199 impairs severe acute respiratory syndrome coronavirus 2 replication *in vivo*

Given the strong *in vitro* antiviral effects of the PAD4-specific inhibitor GSK199, we next investigated its *in vivo* efficacy. As data on the distribution and bioavailability of PAD inhibitors in peripheral organs of treated mice are lacking, we first determined whether GSK199 and BB-Cl could reach the lung and brain following intraperitoneal administration. For this purpose, organs from inhibitor- and vehicle-treated mice were collected after 7 days of daily treatment, homogenized in RIPA buffer, and analyzed through LC-MS/MS for inhibitor concentration, expressed as [μg of inhibitor/g of organ] (Table S4). As shown in Figures S6A–S6D, GSK199 was detected in both the lungs and brains of all treated animals, whereas BB-Cl was found only in the lungs, where it was detectable in 5 out of the 6 treated animals.

To assess the *in vivo* antiviral activity of the PAD4 inhibitor, K18-hACE2 transgenic mice were infected with the SARS-CoV-2 Delta strain and treated daily via intraperitoneal injection with GSK199 (30 mg/kg),[40] BB-Cl (1 mg/kg),[53] or vehicle control. Treatment started one day prior to infection and continued every day throughout the experiment (Figure 5A). Mice were monitored daily for body weight and clinical score (Figures S7A and S7B). At 4 dpi, a time point when viral loads and histopathological changes were expected to be ongoing based on previous reports,[47] the animals (n = 10/group) were euthanized, nasal swabs were collected, and lungs and brains were harvested. The organs from four animals per group were formalin-fixed and paraffin-embedded for H&E and histopathological analyses, while the remaining six were processed for RNA and protein extraction.

Absolute viral load in lung tissues was quantified via ddPCR. As shown in Figure 5B, GSK199-treated mice had significantly lower lung viral loads than those of vehicle-treated controls—approximately a 100-fold reduction at 4 dpi, 6×10^4 vs. 6×10^2, respectively. In addition, GSK199-treated mice had clearly fewer SARS-CoV-2 infectious

Figure 4. PAD4 inhibition blocks SARS-CoV-2 protein and genome synthesis

(A) Relative viral RNA quantification in cell extracts from SARS-CoV-2-infected Huh7.5 (left) or Calu3 (right) cells (MOI 0.1) treated with GSK199 (20 μM), BB-Cl (5 μM), or DMSO, determined by comparative RT-qPCR. Values are expressed relative to vehicle-treated samples and normalized to the housekeeping gene PGK1. Data represent mean ± SEM from three independent experiments and are analyzed by *t* test. $^*p < 0.05$, $^{**}p < 0.01$, and $^{***}p < 0.001$.

(B) Western blot analysis of viral protein expression in Huh7.5 and Calu3 cells, either mock-infected or infected with SARS-CoV-2 (MOI 0.1) and treated with GSK199 (20 μM), BB-Cl (5 μM), or DMSO. One representative blot from three independent experiments is shown.

(C) Schematic representation of infection and treatment protocols used for the viral entry inhibition assay.

(D) Viral entry assay on VERO-E6 (left) and TMPRSS2-rexpressing VERO-E6 (right) infected with VSV-Spike GFP (MOI 1). GFP-positive infected cells are microscopically counted, and the results are expressed as a percentage relative to vehicle-treated cells, and are analyzed by *t* test. Data represent mean ± SEM.

(E) Absolute quantification of viral RNA released from SARS-CoV-2-infected Huh7.5 (left) or Calu3 (right) cells (MOI 0.1) treated with DMSO (vehicle) or GSK199 (20 μM), either using standard treatment (total) or added at 2 hpi (Post), determined by qRT-PCR. Supernatants are collected at 24 hpi for Calu3 and 48 hpi for Huh7.5. Data represent mean ± SEM from three independent experiments and are analyzed by *t* test. $^*p < 0.05$ and $^{**}p < 0.01$.

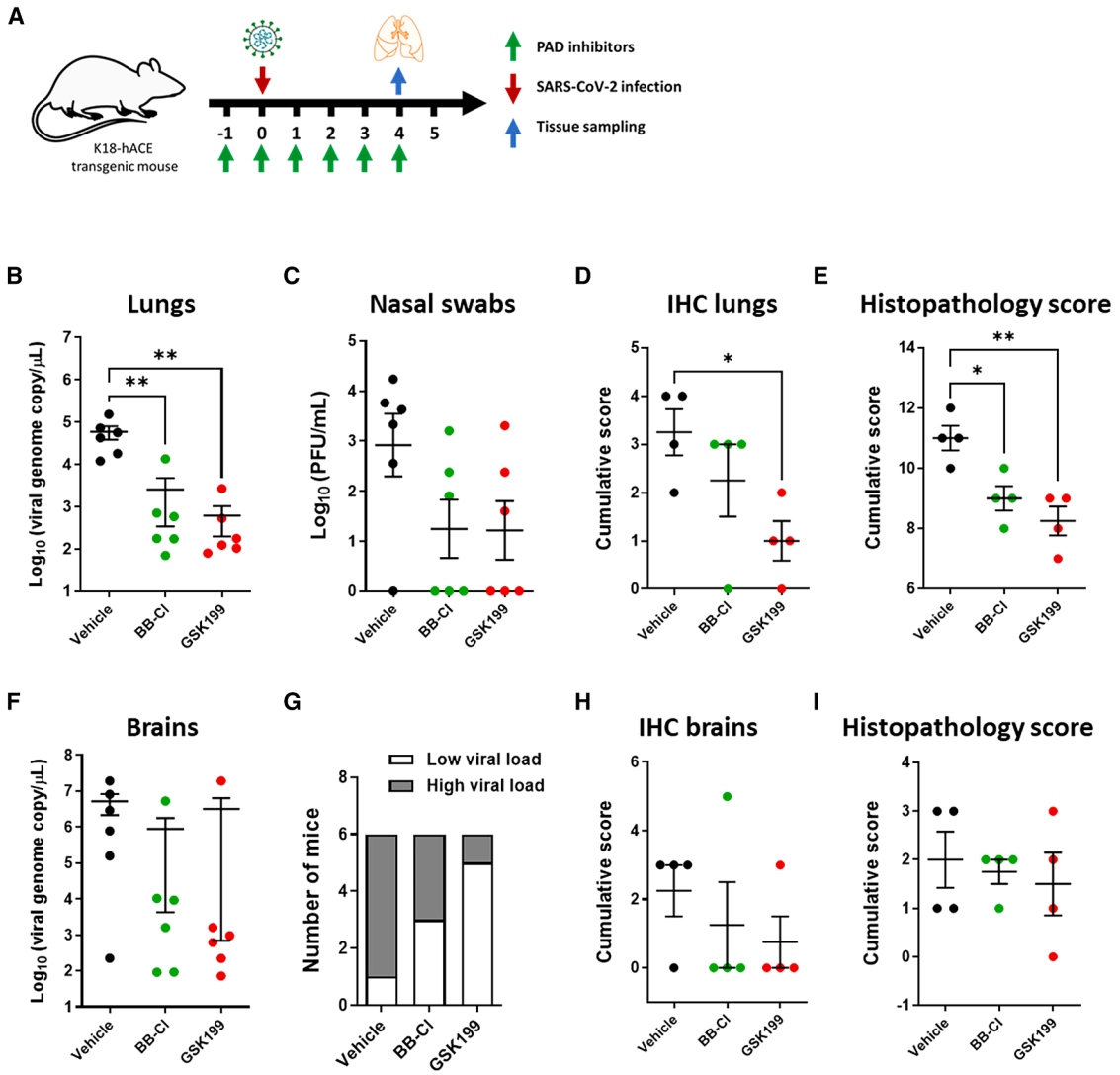

Figure 5. *In vivo* antiviral activity of PAD inhibitors against SARS-CoV-2

(A) Schematic representation of the treatment and infection protocols in K18-hACE2 transgenic mice.

(B) Quantification of viral genome copies in mouse lungs—treated and infected as described in A— by ddPCR. Each dot represents an individual mouse sample (n = 6).

(C) Plaque assay to determine the number of infectious viral particles in mouse nasal swabs.

(D) Graphical representation of cumulative scores from Table 2 for immunohistochemical staining of mouse lungs using an anti-SARS-CoV-2 nucleocapsid antibody (n = 4). Y axis represents the cumulative score calculated according to the criteria described in Table 2.

(E) Graphical representation of cumulative scores from Table 5 for H&E staining of mouse lungs (n = 4), showing histopathological alterations classified by anatomical site and summarized as a percentage of tissue involvement.

(F) Quantification of viral genome copies in mouse brains—treated and infected, as represented in A— by ddPCR. Each dot represents an individual mouse sample (n = 6).

(G) Distribution of brains from vehicle- or PAD-inhibitor-treated infected mice based on viral load (low: < below 10^3; high: > below 10^3).

(H) Graphical representation of cumulative scores from Table 4 for immunohistochemical staining of mouse brains using anti-SARS-CoV-2 nucleocapsid antibody (n = 4). Y axis represents the cumulative score calculated according to the criteria described in Table 4.

(I) Graphical representation of cumulative scores from Table 5 for H&E staining of mouse brains (n = 4), showing histopathological alterations classified by anatomical site and summarized as a percentage of tissue involvement. Data from all experiments, which represent mean ± SEM, are analyzed using an unpaired two-tailed t test. *p < 0.05, **p < 0.01, and ***p < 0.001.

particles in nasal swabs, as judged by virus titration assay (Figure 5C). Immunohistochemistry for viral N protein on lung tissues further revealed a marked reduction in the number of infected cells exclusively in GSK199-treated animals (Figures 5D and S8A; extended data Table 2). Similarly, BB-CI treatment also decreased viral replication and

Table 2. Immunohistochemical analysis of SARS-CoV-2 nucleocapsid protein in murine lung tissue following PAD inhibitor treatment

		BLOOD VESSELS	INTERSTITIUM	AIRWAYS/ALVEOLI			
Treatment	Sample (lung)	Vascular wall/ inflammatory infiltrates	Macrophages/ mononuclear cells	Type I pneumocytes	Type II pneumocytes/ alveolar macrophages	Bronchial/ bronchiolar epithelium	CUMULATIVE SCORE
Vehicle	#751	0	1**	0	1**	0	2
	#752	0	1**	0	2**	0	3
	#753	0	1**	0	2**	1*	4
	#754	0	1**	1**	2**	0	4
BB-Cl	#782	0	1**	0	2**	0	3
	#783	0	1**	0	2**	0	3
	#784	0	1**	1**	1**	0	3
	#785	0	0	0	0	0	0
GSK199	#790	0	0	0	0	0	0
	#791	0	1*	0	0	0	1
	#792	0	1**	0	0	0	1
	#793	0	1*	0	1**	0	2

Scoring criteria: 0: not detected; 1: mild/weak staining; 2: moderate staining; 3: strong staining. Percentage (%) of virus antigen-positive cells: one focal immunolabeled area (*); multifocal immunolabeled areas (**).
BB-Cl, BB-Cl-amidine; GSK199, PAD4-specific inhibitor; K18-hACE2, transgenic mice expressing human angiotensin-converting enzyme 2; SARS-CoV-2, severe acute respiratory syndrome coronavirus 2; IHC, immunohistochemistry.

the number of viral particles in nasal swabs (Figures 5B and 5C), though it was less effective than GSK199 in reducing SARS-CoV-2 nucleoprotein synthesis (Figure 5D), in good agreement with previous immunoblot analyses in Calu3 cells. H&E-stained lung sections revealed diffuse alveolar damage with progressive alveolar, interstitial, and vascular lesions characterized by edema, inflammation, and focal cytomegaly in some alveolar lining cells. When we systematically scored these parameters (Table 3), we found that both pan-PAD and PAD4-specific inhibitors significantly lowered their total cumulative score (Figures 5E and S8C).

Since several studies have reported the presence of SARS-CoV-2 in the brains of mice following intranasal infection,[54] we evaluated the antiviral activity of PAD inhibitors in this tissue. As shown in Figure 5F, brain viral load showed extremely high variability in all groups. However, when samples were categorized into two groups based on their viral load—low (below 10^3) and high (above 10^3)—we observed that only the samples from GSK199-treated mice were more likely to belong to the low viral load group than those from vehicle-treated mice (Figure 5G). Since we previously demonstrated that GSK199 can cross the blood-brain barrier, these findings imply that the drug may effectively limit viral dissemination and replication within the brain.

Immunohistochemical analyses for viral N protein (Figures 5H and S8B; Table 4) and H&E staining (Figures 5I and S8D; Table 5) confirmed this trend. Interestingly, BB-Cl-treated mice also appeared partially protected from brain infection, even though the drug was unable to reach this organ (Figures 5F–5I). This suggests that while BB-Cl does not act directly in brain tissues, it may reduce the risk of brain infection indirectly. A possible explanation is that by limiting viral replication in peripheral tissues, BB-Cl may lower systemic viral load, thereby decreasing the likelihood of virus invasion into the brain.

Peptidyl-arginine deiminases inhibition modulates inflammation and protects against severe acute respiratory syndrome coronavirus 2-induced pathological changes

Several studies have shown that a cytokine and chemokine storm drives a harmful systemic inflammatory response thought to be the primary cause of acute respiratory distress syndrome (ARDS) in patients with COVID-19.[10] Furthermore, an impaired type I IFN response has been observed in COVID-19, followed by increased circulating levels of IL-6 and TNF-α. Moreover, Neufeld et al. found that the SARS-CoV-2 infection of Calu3 cells induces a pro-inflammatory cytokine response.[55] Based on these premises, we sought to test whether PAD inhibitors could modulate this inflammatory storm in our models.

As shown in Figures 6A and 6B, both GSK199 and BB-Cl significantly reduced *IL-6* and *TNF-α* mRNA expression levels in Calu3 cells following SARS-CoV-2 Delta strain infection. Consistently, in SARS-CoV-2–infected K18-hACE2 mice, *IL-6* mRNA expression at 4 dpi was significantly reduced in both lungs and brains of GSK199-treated compared with vehicle-treated group (Figures 6E and S9). *TNF-α* mRNA levels were also significantly reduced by the PAD4 inhibition in the lung, whereas in the brain, they were only slightly affected (Figures 6F and S9). As expected, *IFN-λ*—predominantly associated with epithelial antiviral responses—was the most strongly induced cytokine in infected Calu3 cells, and both GSK199 and BB-Cl significantly decreased its expression compared with vehicle-treated controls, both *in vitro* and *in vivo* (Figures 6D and 6L). Conversely, *IFN-β* expression was significantly reduced only upon GSK199 treatment

Table 3. Lung histopathological features classified by anatomical site and summarized in the percentage of tissue involvement

		SUB-GROSS	BLOOD VESSELS				INTERSTITIUM			AIRWAYS/ALVEOLI						PLEURA		
Treatment	Sample (lung)	% of lung affected	Endothelial activation/ plumping	Vasculitis/ thrombosis	Perivascular edema	Vascular congestion	Neutrophilic infiltration	Lymphoplasmacytic/ histiocytic infiltration	Necrosis	Hemorrhage	Fibrosis	Hyaline membranes	Alveolar edema	Pneumocytes II/ alveolar macrophages	Neutrophilic infiltration	Lymphoplasmacytic histiocytic infiltration	Hyperplasia/ degeneration (necrosis) of bronchiolar/ alveolar epithelium (syncytia)	Pleural involvement	LUNG CUMULATIVE SCORE
Vehicle	#751	70	2	0	0	2	0	1	0	1	0	0	0	3	0	0	1	1	11
	#752	70	2	0	0	3	0	1	0	1	0	0	0	3	0	0	0	0	10
	#753	60	1	0	0	3	0	1	0	1	0	0	0	3	0	0	3	0	12
	#754	50	1	0	0	3	1	2	0	0	0	0	0	2	0	0	2	0	11
BB-Cl	#782	60	0	0	0	2	1	2	0	0	0	0	0	3	0	0	2	0	10
	#783	60	0	0	0	3	1	1	0	0	0	0	0	3	0	0	1	0	9
	#784	60	0	0	0	4	1	0	0	0	0	0	0	3	0	0	0	1	9
	#785	70	0	0	0	1	0	1	0	0	0	0	0	4	0	0	1	1	8
GSK199	#790	70	0	0	0	1	0	1	0	0	0	0	0	4	0	0	1	1	8
	#791	30	0	0	0	4	1	0	0	0	0	0	0	2	0	0	0	0	7
	#792	30	1	0	0	2	2	0	0	0	0	0	0	3	0	0	1	0	9
	#793	40	1	0	0	3	1	0	0	0	0	0	0	2	0	0	1	1	9

Scoring criteria: 0, no tissue involvement (no findings); 1, up to 25% of involved tissue (mild); 2, up to 50% of involved tissue (moderate); 3, up to 75% of involved tissue (severe); 4, up to 100% of involved tissue (massive).
* (asterisk) syncytia.

(Figures 6C and 6H). To assess the adaptive immune response, we assessed *IFN-γ* expression in the lungs, which was downregulated in GSK199-treated mice relative to vehicle controls (Figure 6I). Finally, we measured *IL-10*, an anti-inflammatory cytokine that—despite its regulatory nature—is persistently elevated in patients with severe COVID-19, correlating with high viral load and lung injury. Similarly, *IL-10* expression was markedly increased in infected K18-hACE2 mice at 4 dpi, and both PAD inhibitors were able to restore its levels toward baseline (Figure 6G). Together, these findings indicate that PAD inhibition broadly attenuates pro-inflammatory and antiviral cytokine responses, highlighting its dual ability to limit both viral replication and excessive immune activation during SARS-CoV-2 infection.

To further characterize the protective effects of PAD inhibition against the pathological changes induced by SARS-CoV-2 infection, we compared citrullination patterns between untreated infected mice and those treated with PAD inhibitors at 4 dpi using mass spectrometry. In agreement with the lung citrullinome analysis at 6 dpi (Figure 2E), we observed a striking alteration in the citrullinome of SARS-CoV-2-infected mice compared to uninfected controls, with over 270 differentially citrullinated proteins (Figure 7A). Among the most over-citrullinated proteins, we identified cytoskeletal proteins, such as MYH1 and the calcium transporter AT2A1, further confirming the pivotal role of citrullination of these proteins, regardless of the post-infection time point. As shown in Figures 7B and 7C, treatment with PAD inhibitors reduced infection-induced over-citrullination. Specifically, citrullination levels of AT2A1 and MYH1 were downregulated in the lungs of infected mice treated with BB-Cl (Figure 7B) or GSK199 (Figure 7C), indicating a shift toward a citrullination profile resembling that of uninfected controls.

A comprehensive analysis of the over-citrullinated proteins during infection revealed the presence of FABP4, S100A6, and TTR, proteins implicated in inflammatory diseases such as rheumatoid arthritis and other autoimmune disorders, where their citrullination plays a crucial role in immune dysregulation and disease progression.[31,56,57] Furthermore, at 4 dpi, SARS-CoV-2 infection led to increased citrullination of PPIA—also known as cyclophilin A—a protein associated with pulmonary fibrosis.[58] Comparing citrullination levels across different treatments, we found that treatment with the PAD4-specific inhibitor effectively prevented SARS-CoV-2-induced over-citrullination. In particular, the heatmap shown in Figure 7D shows a clear shift in over-citrullinated proteins toward mock-like citrullination levels upon treatment with PAD inhibitors, underscoring their therapeutic potential in mitigating SARS-CoV-2-driven inflammation.

DISCUSSION

Over the past five years, SARS-CoV-2 infection has sparked significant interest in viral pathogenesis and host immune responses, particularly in the context of protein PTM. We have recently proposed that one such alteration, citrullination, may play a role in the host response to SARS-CoV-2, though the underlying mechanisms and biological implications of this process were not addressed.[23] In this study, we demonstrate

Table 4. Immunohistochemical analysis of SARS-CoV-2 nucleocapsid protein in murine brain tissue following PAD inhibitor treatment

Treatment	Sample (brain)	BLOOD VESSELS	NEURONS	GLIA	WHITE MATTER	CUMULATIVE SCORE
Vehicle	#751	0	0	0	0	0
	#752	0	2**	0	0	2
	#753	0	0	0	0	0
	#754	0	3**	2*	0	5
BB-Cl	#782	0	3*	0	0	3
	#783	0	3*	0	0	3
	#784	0	0	0	0	0
	#785	0	0	0	0	0
GSK199	#790	0	0	0	0	0
	#791	0	0	0	0	0
	#792	0	0	0	0	0
	#793	0	3**	0	0	3

Scoring criteria: 0: not detected; 1: mild/weak staining; 2: moderate staining; 3: strong staining. Percentage (%) of virus antigen-positive cells: one focal immunolabeled area (*); multifocal immunolabeled areas (**).
BB-Cl, BB-Cl-amidine; GSK199, PAD4-specific inhibitor; K18-hACE2, transgenic mice expressing human angiotensin-converting enzyme 2; SARS-CoV-2, severe acute respiratory syndrome coronavirus 2; IHC, immunohistochemistry.

a key role of PAD4 in SARS-CoV-2 pathogenesis, providing novel insights into how citrullination influences viral replication and the ensuing inflammatory response.

Our findings confirm that SARS-CoV-2 infection across multiple strains (i.e., 2020B.1, Delta, Omicron, and XEc) induces a significant increase in PAD4 expression in all tested human cell lines and murine tissues, including the lung and brain. In particular, the observation that PAD4 upregulation occurs in pulmonary epithelial cells, the primary site of SARS-CoV-2 replication, suggests that this virus exerts a direct effect on PAD expression, independent of the inflammation-driven regulation typically observed in other immune cells. Although all three strains seem capable of promoting PAD4 upregulation, the Delta variant appears to induce a more pronounced increase in PAD expression. This may reflect strain-dependent differences in viral replication kinetics and modulation of host transcriptional programs, which are known to vary among SARS-CoV-2 variants and contribute to disease severity.[50,59,60] Importantly, despite these differences, PAD inhibition effectively suppresses viral replication across all tested variants, including recent recombinant lineages such as XEc, indicating that PAD activity represents a conserved host dependency of SARS-CoV-2. This conclusion is further supported by the strong antiviral efficacy of PAD inhibitors, which also significantly reduced viral replication in our *in vivo* model.

Another important observation from this study is the significant downregulation of PAD2 in the brains of SARS-CoV-2-infected

Table 5. Histopathological analysis of SARS-CoV-2-induced brain lesions in murine models following PAD inhibitor treatment

		NEURONAL CHANGES				MENINGES	
Treatment	Sample (brain)	Gliosis	Perivascular cuffing	Degeneration/ spongiosis of white matter	Neuronal degeneration/ Necrosis	Meningeal involvement	CNS CUMULATIVE SCORE
Vehicle	#751	1	0	WM absent	0	0	1
	#752	0	0	WM absent	1	0	1
	#753	1	0	1	1	0	3
	#754	1	0	1	1	0	3
BB-Cl	#782	0	0	1	1	0	2
	#783	0	0	1	0	0	1
	#784	1	0	1	0	0	2
	#785	1	0	1	0	0	2
GSK199	#790	0	0	1	0	0	1
	#791	0	0	2	0	0	2
	#792	0	0	0	0	0	0
	#793	1	0	1	1	0	3

Scoring criteria (percentage of tissue involvement): 0: No tissue involvement (no findings); 1: up to 25% of tissue affected (mild); 2: up to 50% of tissue affected (moderate); 3: up to 75% of tissue affected (severe); 4: up to 100% of tissue affected (massive).
BB-Cl, BB-Cl-amidine; GSK199, PAD4-specific inhibitor; K18-hACE2, transgenic mice expressing human angiotensin-converting enzyme 2; SARS-CoV-2, severe acute respiratory syndrome coronavirus 2; CNS, central nervous system.

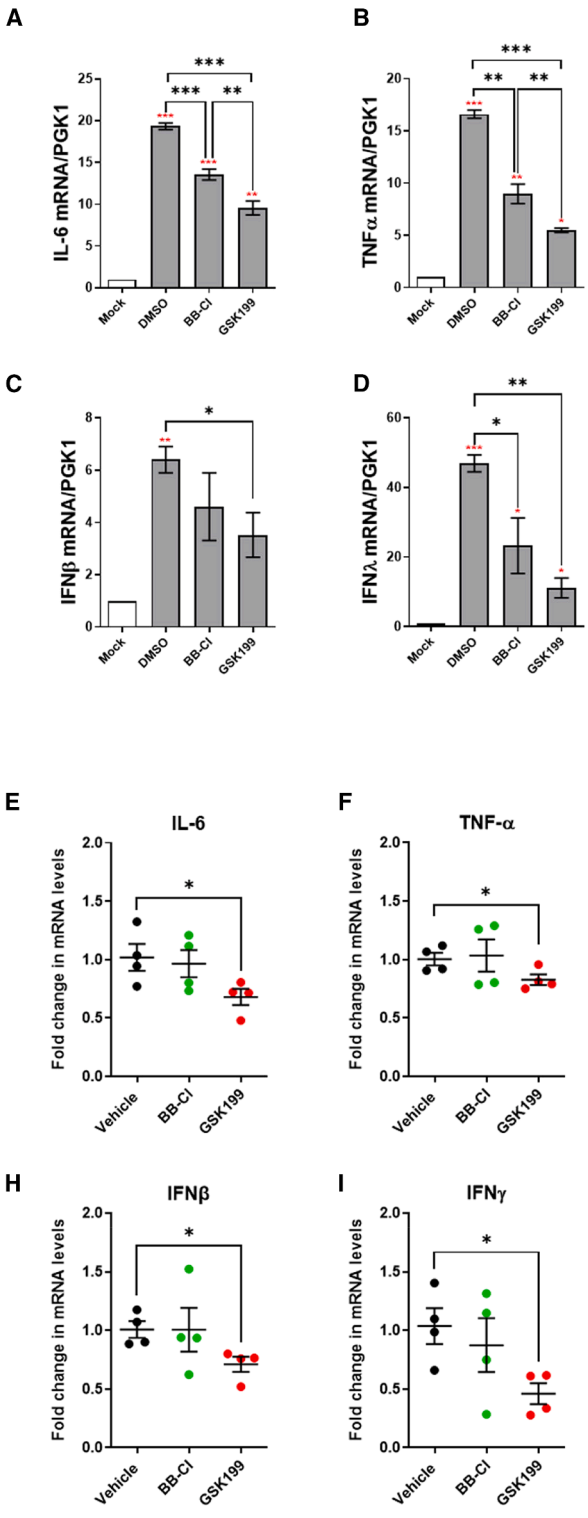

Figure 6. PAD inhibition modulates SARS-CoV-2-induced inflammation

(A–D) Relative mRNA levels of the indicated genes are quantified by comparative RT-qPCR from total RNA of Calu-3 cells infected with the SARS-CoV-2 Delta strain (gray bars; MOI 0.1, 24 hpi) and treated with GSK199 (20 μM), BB-Cl (5 μM), or DMSO (vehicle). Data from three independent experiments were normalized to the housekeeping gene PGK1 and plotted as mean fold change ±SEM over mock-infected cells (white bars). (*$p < 0.05$, **$p < 0.01$, and ***$p < 0.001$; one-way ANOVA followed by Bonferroni's post-test). Red asterisks indicate comparisons with mock control, while black asterisks refer to comparisons among treatments.

(E–J) Relative mRNA levels of the indicated cytokines are quantified by RT-qPCR from lung tissues of mice infected with SARS-CoV-2 Delta variant (10^5 PFU, i.n.) for 4 days and treated with BB-Cl (1 mg/kg), GSK199 (30 mg/kg), or DMSO (vehicle). Each dot represents one individual mouse. Data are normalized to the housekeeping gene β-actin and are presented relative to the mean ΔCt value of vehicle-treated mice. Statistical significance is assessed using an unpaired two-tailed *t* test (*$p < 0.05$, **$p < 0.01$, and ***$p < 0.001$).

mice, a phenomenon that appears to be unique to this organ, as it is not observed to the same extent in the lungs. This finding is particularly intriguing as PAD2 is the most abundantly expressed isoform in the central nervous system (CNS), where it regulates gene expression, neuronal plasticity, and inflammation.[28,48,61] Dysregulation of PAD2 expression or activity has been linked to a variety of neuroinflammatory and neurodegenerative disorders. In multiple sclerosis, for example, reduced PAD2 activity has been associated with disease progression, as citrullination of critical proteins, such as those involved in the neuronal cytoskeleton, is essential for synaptic function and chronic inflammation control.[62,63] The observed downregulation of PAD2 in SARS-CoV-2-infected brains may thus exacerbate neuroinflammation and neurodegenerative damage, potentially contributing to the neurological symptoms reported in patients with COVID-19.[9]

Our findings also point to the critical role of citrullination in SARS-CoV-2 infection. We show that this virus substantially increases the citrullination of specific proteins, likely exploiting this PTM to enhance replication and evade immune detection. Among the most affected proteins, we identify AT2A1, an ATPase responsible for calcium reuptake into the endoplasmic reticulum.[49] Given that elevated cytoplasmic calcium concentrations are critical for SARS-CoV-2 replication,[64,65] AT2A1 dysregulation may represent a deliberate strategy of this virus to hijack host cellular functions. In good

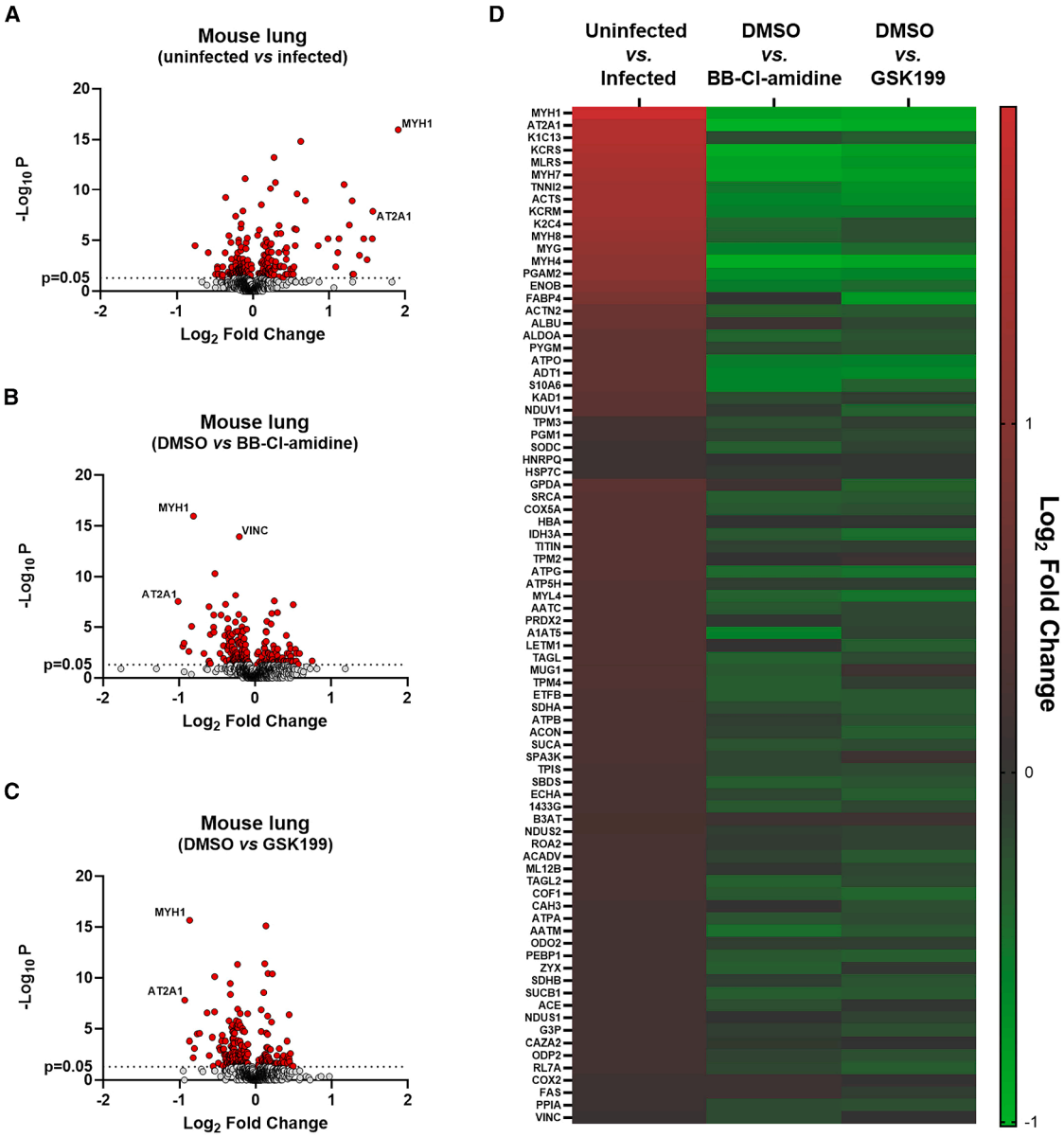

Figure 7. PAD inhibition protects against SARS-CoV-2-induced pathological changes

(A–C) Volcano plots show citrullinated proteins in pooled protein lysates from SARS-CoV-2- vs. mock-infected mouse lungs at 4 dpi. Lysates are incubated with biotin-PG to isolate citrullinated proteins on streptavidin agarose, followed by on-bead tryptic digestion and LC-MS/MS analysis. Each dot represents an identified citrullinated protein. The x axis shows the citrullination ratio between mock and infected samples (A) and between infected mice treated with vehicle (DMSO) or with PAD inhibitors BB-Cl-amidine (B) or GSK199 (C), while the y axis indicates statistical significance, both on a logarithmic scale (n = 3).

(D) Heatmap shows the fold changes of differentially citrullinated proteins identified in lung tissues across the indicated pairwise comparisons: uninfected vs. infected, and vehicle-treated infected vs. BB-Cl–treated or GSK199–treated infected mice. The color scale represents relative citrullination levels expressed as $\log_2$ fold change.

agreement, De Antonellis et al. have shown that SARS-CoV-2 inhibits AT2A1 transcription to sustain high cytoplasmic calcium levels, which favors viral replication.[66] Our findings suggest that the citrullination of AT2A1 further disrupts its ATPase function, impairing calcium clearance and sustaining an intracellular environment conducive to viral replication. Given that PAD enzymes are calcium-dependent, this dysregulation likely establishes a positive feedback loop, where increased PAD activity exacerbates citrullination, thereby favoring viral replication.

In addition to AT2A1, we report increased citrullination of a number of proteins involved in immune functions, such as inflammatory responses and immune cells-extracellular matrix interactions, a phenomenon that we believe may have profound implications for COVID-19 pathogenesis. Citrullinated proteins

are, in fact, recognized as danger-associated molecular patterns (DAMPs), which attract immune cells and may contribute to chronic inflammation and autoimmune disease development.[67] Our findings indicate that SARS-CoV-2 infection induces citrullination in proteins specifically involved in the onset of inflammatory and autoimmune diseases (e.g., FABP4, S100A6, TTR, and PPIA).[56–58] Thus, it is tempting to speculate that these changes may drive both acute symptoms and long-term complications, such as long COVID.

PAD inhibitors demonstrably suppress aberrant citrullination, effectively restoring a protein citrullination profile akin to that of uninfected tissues. Recent genomic studies have identified distinct *PADI4* and *PADI2* haplotypes as genetic determinants of COVID-19 severity,[68,69] underscoring the significance of polymorphisms within the *PAD* gene family in modulating disease severity and progression. In particular, *PADI4* plays a key role in immune regulation, with certain haplotypes correlating with elevated circulating PAD4 levels—a biomarker associated with increased risk of requiring invasive mechanical ventilation in severe ARDS secondary to SARS-CoV-2 pneumonia.[69] Thus, in light of the above, it is possible that the identification of patients with COVID-19 with PAD-related genetic susceptibility may lead to more refined treatment approaches.

Regarding the therapeutic potential of PAD inhibitors, our results show that the PAD4 inhibitor GSK199, following i.p. injection, can cross the blood-brain barrier and exert its effects within the CNS. In contrast, the pan-PAD inhibitor BB-Cl-amidine remains confined to peripheral tissues, such as the lungs, unable to penetrate the blood-brain barrier. Despite their high molecular weight—a characteristic that typically limits blood-brain barrier permeability—these compounds exhibit distinct structural and mechanistic properties: GSK199 acts as a reversible inhibitor, whereas BB-Cl-amidine acts irreversibly. These differences, along with metabolic stability and clearance, likely influence the pharmacokinetic profiles of both compounds. In this regard, it is worth pointing out that the two molecules were administered at different doses in our study, which may have affected their detectability in addition to their intrinsic pharmacological properties. Thus, further studies are needed to elucidate these parameters, which are crucial for the clinical translation of these compounds.

In conclusion, our findings establish citrullination as a key mechanism in SARS-CoV-2 pathogenesis, with profound implications for immune modulation and the development of autoimmune disorders. Our results complement and extend the study by Bonilha et al.,[70] which demonstrated that PAD4 inhibition reduces lung NET accumulation and improves clinical outcomes in infected mice. However, their work did not explore intracellular aspects such as PAD expression dynamics during infection, the impact of PAD inhibition on viral replication, or infection-induced changes in the global citrullination profile. Further investigation is warranted to clarify its precise role in COVID-19 progression and to identify novel therapeutic strategies addressing post-viral complications. Importantly, our study demonstrates the dual efficacy of PAD4 inhibition in both suppressing viral replication and preventing excessive protein citrullination associated with inflammatory pathologies. This interplay further supports the viability of PAD4 inhibitors as therapeutic agents for managing both acute and long-term sequelae of SARS-CoV-2 infection.

Limitations of the study

While this work provides mechanistic and functional evidence linking PAD activity to SARS-CoV-2 pathogenesis, several aspects remain outside its scope. The mass spectrometry dataset highlights proteins whose citrullination is altered during infection, but further studies will be needed to define the precise functional consequences of these modifications. Although two PAD inhibitors were evaluated, a comprehensive pharmacokinetic and structure-activity comparison was beyond the aims of this study. For *in vivo* experiments, we employed the K18-hACE2 mouse model with intranasal viral inoculation, a widely used and well-established system for studying SARS-CoV-2 pathogenesis and antiviral interventions; however, it may not fully capture all features of physiological respiratory infection in humans, particularly with respect to viral dissemination dynamics and tissue tropism. Finally, validation in patient-derived samples and longitudinal clinical settings will be important to further extend the translational relevance of these findings.

RESOURCE AVAILABILITY

Lead contact

Requests for further information and resources should be directed to and will be fulfilled by the lead contact, Marco De Andrea (marco.deandrea@unito.it).

Materials availability

This study did not generate new unique reagents.

Data and code availability

- The mass spectrometry proteomics data generated in this study have been deposited in the ProteomeXchange Consortium via the PRIDE partner repository and are publicly available under the accession number PXD072601 (https://www.ebi.ac.uk/pride/archive/projects/PXD072601), as reported in the key resources table.
- This study did not generate new code.
- Any additional information required to reanalyze the data reported in this article is available from the lead contact upon request.

ACKNOWLEDGMENTS

We thank Marcello Arsura for critically reviewing the manuscript. This research was supported by EU funding within the NextGeneration EU-MUR PNRR Extended Partnership initiative on Emerging Infectious Diseases (Project no. PE00000007, INF-ACT to M.D.A., S.R. and I.F.), and by the European Virus Archive GLOBAL (EVA-GLOBAL) project that has received funding from the European Union's Horizon 2020 research and innovation program under grant agreement No. 871029, which provided access to SARS-CoV-2 Delta isolate (hCoV-19/Netherlands/NH-RIVM-27142/2021_P2). This research was also supported by the University of Turin (RILO2023 and RILO2024 to M.D.A. and F.G.), the Ministry of Education, University and Research—MUR (PRIN Project 2022 HERMIA to S.D.; PRIN Project PNRR 2022 P20225P4T7 to L.S.), the Caterpillar Foundation (ROSA_CARIVARI20_01 to A.R.), and the National Institutes of Health (grant R35 GM118112 to P.R.T.). Selina Pasquero was supported by "Istituto di Ricerca Virologica Orietta Bartolomei Corsi," Florence - Italy. Alessandro Penna was supported by Fondazione Umberto Veronesi. The funders had no role in study design, data collection and analysis, decision to publish, or preparation of this manuscript.

AUTHOR CONTRIBUTIONS

S.P. and M.D.A. supervised and coordinated the project, contributed to visualization, funding acquisition, and editing of the final manuscript. S.P. conceived the study, developed the methodology, performed formal analyses and experiments, curated the data, and wrote the original draft. L.S. and S.D. contributed to methodology development, conducted experiments, and revised the manuscript. F.G. and V.C. were responsible for data validation; V.C. also contributed to experimental work, while F.G. contributed to manuscript review and editing. A.D.P., B.G., A.R., and A.P. conducted *in vivo* experiments, including infection, treatment, and tissue collection, and contributed to manuscript revision. R.V. and S.T. performed histological and immunohistochemical analyses. F.F. performed transcriptomic data analysis. W.C., R.M.G., and P.R.T. carried out mass spectrometry experiments, processed the corresponding raw data, and contributed to manuscript editing. I.F. and S.N.R. conducted plaque assays on nasal swabs and revised the manuscript. A.T. performed multiplex immunofluorescence and contributed to manuscript editing. E.D.G. and S.V. quantified inhibitors in murine tissues and curated the related data.

DECLARATION OF INTERESTS

The authors declare no competing interests.

STAR★METHODS

Detailed methods are provided in the online version of this paper and include the following:

- KEY RESOURCES TABLE
- EXPERIMENTAL MODEL AND STUDY PARTICIPANT DETAILS
  - Cell lines and viruses
  - Animal studies
- METHOD DETAILS
  - Reagents and treatments
  - Cell viability assay
  - *In vitro* antiviral assay
  - Quantitative real-time qRT-PCR (viral load)
  - Plaque assay
  - RNA isolation and comparative qRT-PCR
  - Droplet Digital PCR (ddPCR)
  - Western blot analysis
  - Detection of citrullination with rhodamine-phenylglyoxal (Rh-PG)
  - Neutralization assay
  - SARS-CoV-2 recovery from nasopharyngeal swabs and titration
  - Histology and immunohistochemistry
  - Multiplex immunofluorescence
  - Liquid-liquid extraction of inhibitors from lung and brain homogenates
  - LC-HRMS analyses
  - Citrullinome analysis by mass spectrometry: Sample preparation
  - Mass spectrometry
  - Database search
  - Ethics approval statement
- QUANTIFICATION AND STATISTICAL ANALYSIS

SUPPLEMENTAL INFORMATION

Supplemental information can be found online at https://doi.org/10.1016/j.isci.2026.115038.

Received: June 9, 2025
Revised: November 12, 2025
Accepted: February 12, 2026
Published: February 17, 2026

REFERENCES

1. Xu, Z., Shi, L., Wang, Y., Zhang, J., Huang, L., Zhang, C., Liu, S., Zhao, P., Liu, H., Zhu, L., et al. (2020). Pathological findings of COVID-19 associated with acute respiratory distress syndrome. Lancet Respir. Med. *8*, 420–422. https://doi.org/10.1016/S2213-2600(20)30076-X.
2. Lu, R., Zhao, X., Li, J., Niu, P., Yang, B., Wu, H., Wang, W., Song, H., Huang, B., Zhu, N., et al. (2020). Genomic characterisation and epidemiology of 2019 novel coronavirus: implications for virus origins and receptor binding. Lancet *395*, 565–574. https://doi.org/10.1016/S0140-6736(20)30251-8.
3. Beigel, J.H., Tomashek, K.M., Dodd, L.E., Mehta, A.K., Zingman, B.S., Kalil, A.C., Hohmann, E., Chu, H.Y., Luetkemeyer, A., Kline, S., et al. (2020). Remdesivir for the Treatment of Covid-19 — Final Report. N. Engl. J. Med. *383*, 1813–1826. https://doi.org/10.1056/nejmoa2007764.
4. Fischer, W.A., Eron, J.J., Holman, W., Cohen, M.S., Fang, L., Szewczyk, L.J., Sheahan, T.P., Baric, R., Mollan, K.R., Wolfe, C.R., et al. (2022). A phase 2a clinical trial of molnupiravir in patients with COVID-19 shows accelerated SARS-CoV-2 RNA clearance and elimination of infectious virus. Sci. Transl. Med. *14*, eabl7430. https://doi.org/10.1126/scitranslmed.abl7430.
5. Rahman, M.M., Masum, M.H.U., Wajed, S., and Talukder, A. (2022). A comprehensive review on COVID-19 vaccines: development, effectiveness, adverse effects, distribution and challenges. Virus Dis. *33*, 1–22. https://doi.org/10.1007/s13337-022-00755-1.
6. COVID-19 epidemiological update – 14 March 2025. https://www.who.int/publications/m/item/covid-19-epidemiological-update-edition-177.
7. Sherif, Z.A., Gomez, C.R., Connors, T.J., Henrich, T.J., and Reeves, W.B.; RECOVER Mechanistic Pathway Task Force (2023). Pathogenic mechanisms of post-acute sequelae of SARS-CoV-2 infection (PASC). eLife *12*, e86002–e86031. https://doi.org/10.7554/elife.86002.
8. Huang, C., Wang, Y., Li, X., Ren, L., Zhao, J., Hu, Y., Zhang, L., Fan, G., Xu, J., Gu, X., et al. (2020). Clinical features of patients infected with 2019 novel coronavirus in Wuhan, China. Lancet *395*, 497–506. https://doi.org/10.1016/S0140-6736(20)30183-5.
9. Tyagi, K., Rai, P., Gautam, A., Kaur, H., Kapoor, S., Suttee, A., Jaiswal, P.K., Sharma, A., Singh, G., and Barnwal, R.P. (2023). Neurological manifestations of SARS-CoV-2: complexity, mechanism and associated disorders. Eur. J. Med. Res. *28*, 307–325. https://doi.org/10.1186/s40001-023-01293-2.
10. Yang, L., Xie, X., Tu, Z., Fu, J., Xu, D., and Zhou, Y. (2021). The signal pathways and treatment of cytokine storm in COVID-19. Signal Transduct. Target. Ther. *6*, 255. https://doi.org/10.1038/s41392-021-00679-0.
11. Bonaventura, A., Vecchié, A., Dagna, L., Martinod, K., Dixon, D.L., Van Tassell, B.W., Dentali, F., Montecucco, F., Massberg, S., Levi, M., and Abbate, A. (2021). Endothelial dysfunction and immunothrombosis as key pathogenic mechanisms in COVID-19. Nat. Rev. Immunol. *21*, 319–329. https://doi.org/10.1038/s41577-021-00536-9.
12. Sun, Y., Jin, L., Dian, Y., Shen, M., Zeng, F., Chen, X., and Deng, G. (2023). Oral Azvudine for hospitalised patients with COVID-19 and pre-existing conditions: a retrospective cohort study. eClinicalMedicine *59*, 101981. https://doi.org/10.1016/j.eclinm.2023.101981.
13. Owen, D.R., Allerton, C.M.N., Anderson, A.S., Aschenbrenner, L., Avery, M., Berritt, S., Boras, B., Cardin, R.D., Carlo, A., Coffman, K.J., et al. (2021). An oral SARS-CoV-2 M Mpro inhibitor clinical candidate for the treatment of COVID-19. Science *374*, 1586–1593. https://doi.org/10.1126/science.abl4784.
14. Unoh, Y., Uehara, S., Nakahara, K., Nobori, H., Yamatsu, Y., Yamamoto, S., Maruyama, Y., Taoda, Y., Kasamatsu, K., Suto, T., et al. (2022). Discovery of S-217622, a Noncovalent Oral SARS-CoV-2 3CL Protease Inhibitor Clinical Candidate for Treating COVID-19. J. Med. Chem. *65*, 6499–6512. https://doi.org/10.1021/acs.jmedchem.2c00117.
15. Gandhi, S., Klein, J., Robertson, A.J., Peña-Hernández, M.A., Lin, M.J., Roychoudhury, P., Lu, P., Fournier, J., Ferguson, D., Mohamed Bakhash, S.A.K., et al. (2022). De novo emergence of a remdesivir resistance

mutation during treatment of persistent SARS-CoV-2 infection in an immunocompromised patient: a case report. Nat. Commun. *13*, 1547. https://doi.org/10.1038/s41467-022-29104-y.

16. Iketani, S., Mohri, H., Culbertson, B., Hong, S.J., Duan, Y., Luck, M.I., Annavajhala, M.K., Guo, Y., Sheng, Z., Uhlemann, A.C., et al. (2023). Multiple pathways for SARS-CoV-2 resistance to nirmatrelvir. Nature *613*, 558–564. https://doi.org/10.1038/s41586-022-05514-2.
17. Wang, Q., Iketani, S., Li, Z., Liu, L., Guo, Y., Huang, Y., Bowen, A.D., Liu, M., Wang, M., Yu, J., et al. (2023). Alarming antibody evasion properties of rising SARS-CoV-2 BQ and XBB subvariants. Cell *186*, 279–286.e8. https://doi.org/10.1016/j.cell.2022.12.018.
18. Qu, P., Evans, J.P., Faraone, J.N., Zheng, Y.M., Carlin, C., Anghelina, M., Stevens, P., Fernandez, S., Jones, D., Lozanski, G., et al. (2023). Enhanced neutralization resistance of SARS-CoV-2 Omicron subvariants BQ.1, BQ.1.1, BA.4.6, BF.7, and BA.2.75.2. Cell Host Microbe *31*, 9–17.e3. https://doi.org/10.1016/j.chom.2022.11.012.
19. Kumar, R., Mehta, D., Mishra, N., Nayak, D., and Sunil, S. (2020). Role of host-mediated post-translational modifications (PTMS) in RNA virus pathogenesis. Int. J. Mol. Sci. *22*, 323–326. https://doi.org/10.3390/ijms22010323.
20. Pratesi, F., Tommasi, C., Anzilotti, C., Chimenti, D., and Migliorini, P. (2006). Deiminated Epstein-Barr virus nuclear antigen 1 is a target of anti-citrullinated protein antibodies in rheumatoid arthritis. Arthritis Rheum. *54*, 733–741. https://doi.org/10.1002/art.21629.
21. Casanova, V., Sousa, F.H., Shakamuri, P., Svoboda, P., Buch, C., D'Acremont, M., Christophorou, M.A., Pohl, J., Stevens, C., and Barlow, P.G. (2020). Citrullination Alters the Antiviral and Immunomodulatory Activities of the Human Cathelicidin LL-37 During Rhinovirus Infection. Front. Immunol. *11*, 85. https://doi.org/10.3389/fimmu.2020.00085.
22. Griffante, G., Gugliesi, F., Pasquero, S., Dell'Oste, V., Biolatti, M., Salinger, A.J., Mondal, S., Thompson, P.R., Weerapana, E., Lebbink, R.J., et al. (2021). Human cytomegalovirus-induced host protein citrullination is crucial for viral replication. Nat. Commun. *12*, 3910. https://doi.org/10.1038/s41467-021-24178-6.
23. Pasquero, S., Gugliesi, F., Griffante, G., Dell'Oste, V., Biolatti, M., Albano, C., Bajetto, G., Delbue, S., Signorini, L., Dolci, M., et al. (2022). Novel antiviral activity of PAD inhibitors against human beta-coronaviruses HCoV-OC43 and SARS-CoV-2. Antiviral Res. *200*, 105278. https://doi.org/10.1016/j.antiviral.2022.105278.
24. Fanelli, I., Rovero, P., Hansen, P.R., Frederiksen, J.L., Houen, G., and Trier, N.H. (2022). Reactivity of Rheumatoid Arthritis-Associated Citrulline-Dependent Antibodies to Epstein-Barr Virus Nuclear Antigen1-3. Antibodies *11*, 15–20. https://doi.org/10.3390/antib11010020.
25. Pasquero, S., Gugliesi, F., Biolatti, M., Dell'Oste, V., Albano, C., Bajetto, G., Griffante, G., Trifirò, L., Brugo, B., Raviola, S., et al. (2023). Citrullination profile analysis reveals peptidylarginine deaminase 3 as an HSV-1 target to dampen the activity of candidate antiviral restriction factors. PLoS Path *19*, e1011849. https://doi.org/10.1371/journal.ppat.1011849.
26. Vossenaar, E.R., Zendman, A.J.W., Van Venrooij, W.J., and Pruijn, G.J.M. (2003). PAD, a growing family of citrullinating enzymes: Genes, features and involvement in disease. Bioessays *25*, 1106–1118. https://doi.org/10.1002/bies.10357.
27. Yu, K., and Proost, P. (2022). Insights into peptidylarginine deiminase expression and citrullination pathways. Trends Cell Biol. *32*, 746–761. https://doi.org/10.1016/j.tcb.2022.01.014.
28. Falcão, A.M., Meijer, M., Scaglione, A., Rinwa, P., Agirre, E., Liang, J., Larsen, S.C., Heskol, A., Frawley, R., Klingener, M., et al. (2019). PAD2-Mediated Citrullination Contributes to Efficient Oligodendrocyte Differentiation and Myelination. Cell Rep. *27*, 1090–1102.e10. https://doi.org/10.1016/j.celrep.2019.03.108.
29. Christophorou, M.A., Castelo-Branco, G., Halley-Stott, R.P., Oliveira, C.S., Loos, R., Radzisheuskaya, A., Mowen, K.A., Bertone, P., Silva, J.C.R., Zernicka-Goetz, M., et al. (2014). Citrullination regulates pluripotency and histone H1 binding to chromatin. Nature *507*, 104–108. https://doi.org/10.1038/nature12942.
30. Neeli, I., Khan, S.N., and Radic, M. (2008). Histone deimination as a response to inflammatory stimuli in neutrophils. J. Immunol. *180*, 1895–1902. https://doi.org/10.4049/jimmunol.180.3.1895.
31. Tilvawala, R., Nguyen, S.H., Maurais, A.J., Nemmara, V.V., Nagar, M., Salinger, A.J., Nagpal, S., Weerapana, E., and Thompson, P.R. (2018). The Rheumatoid Arthritis-Associated Citrullinome. Cell Chem. Biol. *25*, 691–704.e6. https://doi.org/10.1016/j.chembiol.2018.03.002.
32. Yuzhalin, A.E. (2019). Citrullination in Cancer. Cancer Res. *79*, 1274–1284. https://doi.org/10.1158/0008-5472.CAN-18-2797.
33. Caprariello, A.V., Rogers, J.A., Morgan, M.L., Hoghooghi, V., Plemel, J.R., Koebel, A., Tsutsui, S., Dunn, J.F., Kotra, L.P., Ousman, S.S., et al. (2018). Biochemically altered myelin triggers autoimmune demyelination. Proc. Natl. Acad. Sci. USA *115*, 5528–5533. https://doi.org/10.1073/pnas.1721115115.
34. Ciesielski, O., Biesiekierska, M., Panthu, B., Soszyński, M., Pirola, L., and Balcerczyk, A. (2022). Citrullination in the pathology of inflammatory and autoimmune disorders: recent advances and future perspectives. Cell. Mol. Life Sci. *79*, 20–94. https://doi.org/10.1007/s00018-022-04126-3.
35. Knight, J.S., Subramanian, V., O'Dell, A.A., Yalavarthi, S., Zhao, W., Smith, C.K., Hodgin, J.B., Thompson, P.R., and Kaplan, M.J. (2015). Peptidylarginine deiminase inhibition disrupts NET formation and protects against kidney, skin and vascular disease in lupus-prone MRL/*lpr* mice. Ann. Rheum. Dis. *74*, 2199–2206. https://doi.org/10.1136/annrheumdis-2014-205365.
36. Willis, V.C., Gizinski, A.M., Banda, N.K., Causey, C.P., Knuckley, B., Cordova, K.N., Luo, Y., Levitt, B., Glogowska, M., Chandra, P., et al. (2011). N-α-Benzoyl-N5-(2-Chloro-1-Iminoethyl)-l-Ornithine Amide, a Protein Arginine Deiminase Inhibitor, Reduces the Severity of Murine Collagen-Induced Arthritis. J. Immunol. *186*, 4396–4404. https://doi.org/10.4049/jimmunol.1001620.
37. Lewis, H.D., Liddle, J., Coote, J.E., Atkinson, S.J., Barker, M.D., Bax, B.D., Bicker, K.L., Bingham, R.P., Campbell, M., Chen, Y.H., et al. (2015). Inhibition of PAD4 activity is sufficient to disrupt mouse and human NET formation. Nat. Chem. Biol. *11*, 189–191. https://doi.org/10.1038/nchembio.1735.
38. Martín Monreal, M.T., Rebak, A.S., Massarenti, L., Mondal, S., Šenolt, L., Ødum, N., Nielsen, M.L., Thompson, P.R., Nielsen, C.H., and Damgaard, D. (2021). Applicability of Small-Molecule Inhibitors in the Study of Peptidyl Arginine Deiminase 2 (PAD2) and PAD4. Front. Immunol. *12*, 1–11. https://doi.org/10.3389/fimmu.2021.716250.
39. Biron, B.M., Chung, C.-S., O'brien, X.M., Chen, Y., Reichner, J.S., and Ayala, A. (2017). Cl-Amidine Prevents Histone 3 Citrullination and Neutrophil Extracellular Trap Formation, and Improves Survival in a Murine Sepsis Model. J. Innate Immun. *9*, 22–32. https://doi.org/10.1159/000448808.
40. Willis, V.C., Banda, N.K., Cordova, K.N., Chandra, P.E., Robinson, W.H., Cooper, D.C., Lugo, D., Mehta, G., Taylor, S., Tak, P.P., et al. (2017). Protein arginine deiminase 4 inhibition is sufficient for the amelioration of collagen-induced arthritis. Clin. Exp. Immunol. *188*, 263–274. https://doi.org/10.1111/cei.12932.
41. Zuo, Y., Yalavarthi, S., Shi, H., Gockman, K., Zuo, M., Madison, J.A., Blair, C., Weber, A., Barnes, B.J., Egeblad, M., et al. (2020). Neutrophil extracellular traps in COVID-19. JCI Insight *5*, e138999. https://doi.org/10.1172/jci.insight.138999.
42. Zhou, Y., Xu, Z., and Liu, Z. (2022). Impact of Neutrophil Extracellular Traps on Thrombosis Formation: New Findings and Future Perspective. Front. Cell. Infect. Microbiol. *12*, 910908–910910. https://doi.org/10.3389/fcimb.2022.910908.
43. Veras, F.P., Pontelli, M.C., Silva, C.M., Toller-Kawahisa, J.E., de Lima, M., Nascimento, D.C., Schneider, A.H., Caetité, D., Tavares, L.A., Colón, D., et al. (2020). SARS-CoV-2 triggered neutrophil extracellular traps (NETs)

mediate COVID-19 pathology. J. Exp. Med. *217*, e20201129. https://doi.org/10.1084/jem.20201129.

44. Thair, S.A., He, Y.D., Hasin-Brumshtein, Y., Sakaram, S., Pandya, R., Toh, J., Rawling, D., Remmel, M., Coyle, S., Dalekos, G.N., et al. (2021). Transcriptomic similarities and differences in host response between SARS-CoV-2 and other viral infections. iScience *24*, 101947. https://doi.org/10.1016/j.isci.2020.101947.
45. Wang, S., Yao, X., Ma, S., Ping, Y., Fan, Y., Sun, S., He, Z., Shi, Y., Sun, L., Xiao, S., et al. (2021). A single-cell transcriptomic landscape of the lungs of patients with COVID-19. Nat. Cell Biol. *23*, 1314–1328. https://doi.org/10.1038/s41556-021-00796-6.
46. Delorey, T.M., Ziegler, C.G.K., Heimberg, G., Normand, R., Yang, Y., Segerstolpe, Å., Abbondanza, D., Fleming, S.J., Subramanian, A., Montoro, D.T., et al. (2021). COVID-19 tissue atlases reveal SARS-CoV-2 pathology and cellular targets. Nature *595*, 107–113. https://doi.org/10.1038/s41586-021-03570-8.
47. Frasson, I., Diamante, L., Zangrossi, M., Carbognin, E., Pietà, A.D., Penna, A., Rosato, A., Verin, R., Torrigiani, F., Salata, C., et al. (2024). Identification of druggable host dependency factors shared by multiple SARS-CoV-2 variants of concern. J. Mol. Cell Biol. *16*, mjae004–mjae015. https://doi.org/10.1093/jmcb/mjae004.
48. Shimada, N., Handa, S., Uchida, Y., Fukuda, M., Maruyama, N., Asaga, H., Choi, E.K., Lee, J., and Ishigami, A. (2010). Developmental and age-related changes of peptidylarginine deiminase 2 in the mouse brain. J. Neurosci. Res. *88*, 798–806. https://doi.org/10.1002/jnr.22255.
49. Chami, M., Gozuacik, D., Lagorce, D., Brini, M., Falson, P., Peaucellier, G., Pinton, P., Lecoeur, H., Gougeon, M.L., Le Maire, M., et al. (2001). SERCA1 truncated proteins unable to pump calcium reduce the endoplasmic reticulum calcium concentration and induce apoptosis. J. Cell Biol. *153*, 1301–1314. https://doi.org/10.1083/jcb.153.6.1301.
50. Saccon, E., Chen, X., Mikaeloff, F., Rodriguez, J.E., Szekely, L., Vinhas, B.S., Krishnan, S., Byrareddy, S.N., Frisan, T., Végvári, Á., et al. (2021). Cell-type-resolved quantitative proteomics map of interferon response against SARS-CoV-2. iScience *24*, 102420. https://doi.org/10.1016/j.isci.2021.102420.
51. Hoffmann, M., Kleine-Weber, H., Schroeder, S., Krüger, N., Herrler, T., Erichsen, S., Schiergens, T.S., Herrler, G., Wu, N.-H., Nitsche, A., et al. (2020). SARS-CoV-2 Cell Entry Depends on ACE2 and TMPRSS2 and Is Blocked by a Clinically Proven Protease Inhibitor. Cell *181*, 271–280.e8. https://doi.org/10.1016/j.cell.2020.02.052.
52. Case, J.B., Rothlauf, P.W., Chen, R.E., Liu, Z., Zhao, H., Kim, A.S., Bloyet, L.-M., Zeng, Q., Tahan, S., Droit, L., et al. (2020). Neutralizing Antibody and Soluble ACE2 Inhibition of a Replication-Competent VSV-SARS-CoV-2 and a Clinical Isolate of SARS-CoV-2. Cell Host Microbe *28*, 475–485.e5. https://doi.org/10.1016/j.chom.2020.06.021.
53. Knight, J.S., Subramanian, V., O'Dell, A.A., Yalavarthi, S., Zhao, W., Smith, C.K., Hodgin, J.B., Thompson, P.R., and Kaplan, M.J. (2015). Peptidylarginine deiminase inhibition disrupts NET formation and protects against kidney, skin and vascular disease in lupus-prone MRL/lpr mice. Ann. Rheum. Dis. *74*, 2199–2206. https://doi.org/10.1136/annrheumdis-2014-205365.
54. Song, E., Zhang, C., Israelow, B., Lu-Culligan, A., Prado, A.V., Skriabine, S., Lu, P., Weizman, O.E., Liu, F., Dai, Y., et al. (2021). Neuroinvasion of SARS-CoV-2 in human and mouse brain. J. Exp. Med. *218*, e20202135. https://doi.org/10.1084/JEM.20202135.
55. Neufeldt, C.J., Cerikan, B., Cortese, M., Frankish, J., Lee, J.Y., Plociennikowska, A., Heigwer, F., Prasad, V., Joecks, S., Burkart, S.S., et al. (2022). SARS-CoV-2 infection induces a pro-inflammatory cytokine response through cGAS-STING and NF-κB. Commun. Biol. *5*, 45. https://doi.org/10.1038/s42003-021-02983-5.
56. Guo, D., Lin, C., Lu, Y., Guan, H., Qi, W., Zhang, H., Shao, Y., Zeng, C., Zhang, R., Zhang, H., et al. (2022). FABP4 secreted by M1-polarized macrophages promotes synovitis and angiogenesis to exacerbate rheumatoid arthritis. Bone Res. *10*, 45. https://doi.org/10.1038/s41413-022-00211-2.
57. Demoruelle, M.K., Harrall, K.K., Ho, L., Purmalek, M.M., Seto, N.L., Rothfuss, H.M., Weisman, M.H., Solomon, J.J., Fischer, A., Okamoto, Y., et al. (2017). Anti-Citrullinated Protein Antibodies Are Associated With Neutrophil Extracellular Traps in the Sputum in Relatives of Rheumatoid Arthritis Patients. Arthritis Rheumatol. *69*, 1165–1175. https://doi.org/10.1002/art.40066.
58. Alqudah, A., AbuDalo, R., Qnais, E., Wedyan, M., Oqal, M., and McClements, L. (2023). The emerging importance of immunophilins in fibrosis development. Mol. Cell. Biochem. *478*, 1281–1291. https://doi.org/10.1007/s11010-022-04591-1.
59. Mautner, L., Hoyos, M., Dangel, A., Berger, C., Ehrhardt, A., and Baiker, A. (2022). Replication kinetics and infectivity of SARS-CoV-2 variants of concern in common cell culture models. Virol. J. *19*, 76. https://doi.org/10.1186/s12985-022-01802-5.
60. Tanneti, N.S., Patel, A.K., Tan, L.H., Marques, A.D., Perera, R.A.P.M., Sherrill-Mix, S., Kelly, B.J., Renner, D.M., Collman, R.G., Rodino, K., et al. (2024). Comparison of SARS-CoV-2 variants of concern in primary human nasal cultures demonstrates Delta as most cytopathic and Omicron as fastest replicating. mBio *15*, e0312923. https://doi.org/10.1128/mbio.03129-23.
61. Lee, C.Y., Wang, D., Wilhelm, M., Zolg, D.P., Schmidt, T., Schnatbaum, K., Reimer, U., Pontén, F., Uhlén, M., Hahne, H., et al. (2018). Mining the human tissue proteome for protein citrullination. Mol. Cell. Proteomics *17*, 1378–1391. https://doi.org/10.1074/mcp.RA118.000696.
62. Yang, L., Tan, D., and Piao, H. (2016). Myelin Basic Protein Citrullination in Multiple Sclerosis: A Potential Therapeutic Target for the Pathology. Neurochem. Res. *41*, 1845–1856. https://doi.org/10.1007/s11064-016-1920-2.
63. Schirmer, L., Velmeshev, D., Holmqvist, S., Kaufmann, M., Werneburg, S., Jung, D., Vistnes, S., Stockley, J.H., Young, A., Steindel, M., et al. (2019). Neuronal vulnerability and multilineage diversity in multiple sclerosis. Nature *573*, 75–82. https://doi.org/10.1038/s41586-019-1404-z.
64. Berlansky, S., Sallinger, M., Grabmayr, H., Humer, C., Bernhard, A., Fahrner, M., and Frischauf, I. (2022). Calcium Signals during SARS-CoV-2 Infection: Assessing the Potential of Emerging Therapies. Cells *11*, 253. https://doi.org/10.3390/cells11020253.
65. Poggio, E., Vallese, F., Hartel, A.J.W., Morgenstern, T.J., Kanner, S.A., Rauh, O., Giamogante, F., Barazzuol, L., Shepard, K.L., Colecraft, H.M., et al. (2023). Perturbation of the host cell Ca2+ homeostasis and ER-mitochondria contact sites by the SARS-CoV-2 structural proteins E and M. Cell Death Dis. *14*, 297. https://doi.org/10.1038/s41419-023-05817-w.
66. de Antonellis, P., Ferrucci, V., Miceli, M., Bibbo, F., Asadzadeh, F., Gorini, F., Mattivi, A., Boccia, A., Russo, R., Andolfo, I., et al. (2024). Targeting ATP2B1 impairs PI3K/Akt/FOXO signaling and reduces SARS-COV-2 infection and replication. EMBO Rep. *25*, 2974–3007. https://doi.org/10.1038/s44319-024-00164-z.
67. Alghamdi, M., Alasmari, D., Assiri, A., Mattar, E., Aljaddawi, A.A., Alattas, S.G., and Redwan, E.M. (2019). An overview of the intrinsic role of citrullination in autoimmune disorders. J. Immunol. Res. *2019*, 7592851. https://doi.org/10.1155/2019/7592851.
68. Gutiérrez-Pérez, I.A., Buendía-Roldán, I., Zaragoza-García, O., Pérez-Rubio, G., Villafan-Bernal, J.R., Chávez-Galán, L., Parra-Rojas, I., Hernández-Zenteno, R. de J., Fricke-Galindo, I., Castro-Alarcón, N., et al. (2024). Association of PADI2 and PADI4 polymorphisms in COVID-19 host severity and non-survival. Heliyon *10*, e27997. https://doi.org/10.1016/j.heliyon.2024.e27997.
69. Adriana Gutiérrez-Pérez, I., Pérez-Rubio, G., Rafael Villafan-Bernal, J., Buendía-Roldán, I., Zaragoza-García, O., Chávez-Galán, L., Rosendo-Chalma, P., Fricke-Galindo, I., Falfán-Valencia, R., and Paola Guzmán-Guzmán, I. (2025). Circulating levels of PADs and citrullinated histone H3 in SARS-CoV-2 infection: Influence of genetic polymorphisms. Clin. Chim. Acta *569*, 120180. https://doi.org/10.1016/j.cca.2025.120180.
70. Bonilha, C.S., Veras, F.P., Dos Santos Ramos, A., Gomes, G.F., Rodrigues Lemes, R.M., Arruda, E., Alves-Filho, J.C., Cunha, T.M., and Cunha, F.Q. (2025). PAD4 inhibition impacts immune responses in SARS-CoV-2

infection. Mucosal Immunol. *18*, 861–873. https://doi.org/10.1016/j.mucimm.2025.04.006.

71. Yinda, C.K., Port, J.R., Bushmaker, T., Offei Owusu, I., Purushotham, J.N., Avanzato, V.A., Fischer, R.J., Schulz, J.E., Holbrook, M.G., Hebner, M.J., et al. (2021). K18-hACE2 mice develop respiratory disease resembling severe COVID-19. PLoS Pathog. *17*, e1009195. https://doi.org/10.1371/journal.ppat.1009195.
72. Signorini, L., Dolci, M., Castelnuovo, N., Crespi, L., Incorvaia, B., Bagnoli, P., Parapini, S., Basilico, N., Galli, C., Ambrogi, F., et al. (2022). Longitudinal, virological, and serological assessment of hospitalized COVID-19 patients. J. Neurovirol. *28*, 113–122. https://doi.org/10.1007/s13365-021-01029-0.
73. Amaro, A., Reggiani, F., Fenoglio, D., Gangemi, R., Tosi, A., Parodi, A., Banelli, B., Rigo, V., Mastracci, L., Grillo, F., et al. (2023). Guadecitabine increases response to combined anti-CTLA-4 and anti-PD-1 treatment in mouse melanoma in vivo by controlling T-cells, myeloid derived suppressor and NK cells. J. Exp. Clin. Cancer Res. *42*, 67. https://doi.org/10.1186/s13046-023-02628-x.
74. Perez-Riverol, Y., Bandla, C., Kundu, D.J., Kamatchinathan, S., Bai, J., Hewapathirana, S., John, N.S., Prakash, A., Walzer, M., Wang, S., and Vizcaíno, J.A. (2025). The PRIDE database at 20 years: 2025 update. Nucleic Acids Res. *53*, D543–D553. https://doi.org/10.1093/nar/gkae1011.
75. Keller, A.D., Nesvizhskii, A.I., Kolker, E., and Aebersold, R. (2002). Empirical statistical model to estimate the accuracy of protein identifications made by MS/MS and database search. In Proceedings 50th ASMS Conference on Mass Spectrometry and Allied Topics, *74*, pp. 37–38.
76. Nesvizhskii, A.I., Keller, A., Kolker, E., and Aebersold, R. (2003). A statistical model for identifying proteins by tandem mass spectrometry. Anal. Chem. *75*, 4646–4658. https://doi.org/10.1021/ac0341261.
77. Shadforth, I.P., Dunkley, T.P.J., Lilley, K.S., and Bessant, C. (2005). i-Tracker: For quantitative proteomics using iTRAQ^{TM}. BMC Genom. *6*, 1–6. https://doi.org/10.1186/1471-2164-6-145.
78. Oberg, A.L., and Vitek, O. (2009). Statistical design of quantitative mass spectrometry-based proteomic experiments. J. Proteome Res. *8*, 2144–2156. https://doi.org/10.1021/pr8010099.

STAR★METHODS

KEY RESOURCES TABLE

REAGENT or RESOURCE	SOURCE	IDENTIFIER
Antibodies		
CCP Rabbit Polyclonal Antibody	Biorbyt	Cat# orb10262; RRID:AB_10752577
PADI2 Polyclonal antibody	Proteintech	Cat# 12110-1-AP; RRID:AB_2159475
PADI4/PAD4 polyclonal antibody	Proteintech	Cat# 17373-1-AP; RRID:AB_2878398
anti-actin	Sigma-Aldrich	Cat# A2066; RRID:AB_476693
anti-Nucleoprotein(N)_SARS-CoV-2 [3851]	GeneTex	Cat# GTX36802; RRID:AB_11162302
anti-Spike(S)_SARS-CoV-2 [1A9]	GeneTex	Cat# GTX632604; RRID:AB_2864418
SARS-CoV-1/2 Spike Protein (2B3E5) Mouse Monoclonal Antibody	Cell Signaling	Cat# 52342
ECL Rabbit IgG, HRP-linked whole Ab (from donkey)	Cytiva	Cat# NA934; RRID:AB_772206
ECL Mouse IgG, HRP-linked whole Ab (from sheep)	Cytiva	Cat# NA931; RRID:AB_772210
mouse anti-mouse β-tubulin IV antibody	Sigma-Aldrich	Cat# T7941; RRID:AB_261775
rat anti-mouse F4/80 antibody [cl A3-1]	Bio-Rad Laboratories	Cat# MCA497R; RRID:AB_323279
Anti-Ly6g antibody [EPR22909-135] rabbit monoclonal	Abcam	Cat# ab238132; RRID:AB_2923218
Anti-CD3 antibody [CD3-12] rat monoclonal	Abcam	Cat# ab11089; RRID:AB_2889189
Anti-Cytokeratin 8 antibody [EP1628Y] rabbit monoclonal	Abcam	Cat# ab53280; RRID:AB_869901
ImmPRESS HRP-conjugated Goat Anti-Rabbit IgG Antibody	Vector Laboratories	Cat# MP-7451; RRID:AB_2631198
ImmPRESS HRP-conjugated Goat Anti-Rat IgG Antibody	Vector Laboratories	Cat# MP-7404; RRID:AB_2336531
Bacterial and virus strains		
SARS-CoV-2 strains 2020B.1 isolate	Serena Delbue, University of Milan	GenBank: MT748758.1; GISAID: EPI_ISL_584051
SARS-CoV-2 strain Delta B.1.617.2 isolate	Serena Delbue, University of Milan	GISAID EPI_ISL_6602889
SARS-CoV-2 strain Omicron B.1.1.529, BA.1	Serena Delbue, University of Milan	GISAID EPI_ISL_10898045
SARS-CoV-2 strain XEc XBB.1.5/BA.2.86 isolate	Serena Delbue, University of Milan	GISAID EPI_ISL_19468204
Vesicular stomatitis virus rVSV-eGFP-SARS-CoV-2-SΔ21	Sean P.J. Whelan (Washington University School of Medicine, USA)	BioProject: PRJNA635934; SRA: SRR11878607.
hCoV-19/Netherlands/NH-RIVM-27142/2021_P2 (SARS-CoV-2 Delta variant, lineage B.1.617.2)	European Virus Archive goes Global (EVAg) platform	014V-04279
Chemicals, peptides, and recombinant proteins		
Cl-Amidine (hydrochloride)	Cayman Chemical	Cat# 10599; CAS: 1373232-26-8
BB-Cl-Amidine (trifluoroacetate salt)	Cayman Chemical	Cat# 17079
GSK 199 (hydrochloride)	Cayman Chemical	Cat# 17489; CAS: 1549811-53-1
DMEM - high glucose	Sigma-Aldrich	Cat# D6546
L-Glutamine–Penicillin–Streptomycin solution	Sigma-Aldrich	Cat# G6784
Fetal bovine serum (FBS)	Sigma-Aldrich	Cat# F7524
3-(4,5-dimethylthiazol-2-yl)-2,5-diphenyltetrazolium bromide (MTT)	Sigma-Aldrich	Cat# 475989; CAS: 298-93-1

(*Continued on next page*)

Continued

REAGENT or RESOURCE	SOURCE	IDENTIFIER
TRI Reagent solution	Sigma-Aldrich	Cat# 93289
Tween 20	Sigma-Aldrich	Cat# P1379
Citrulline-specific Probe-rhodamine (Rh-PG)	Cayman Chemical	Cat# 16172; CAS: 2309313-01-5
Citrulline-specific Probe-biotin (biotin-PG)	Cayman Chemical	Cat# 17450; CAS: 2468149-70-2
Trichloroacetic acid	Sigma-Aldrich	Cat# T6399
L-citrulline	Cayman Chemical	Cat# 35648; CAS: 372-75-8
Brilliant blue G-colloidal solution	Sigma-Aldrich	Cat# B8522; CAS: 6104-58-1
Formaldehyde solution	Sigma-Aldrich	Cat# 1040031000; CAS: 50-00-0
DAPI dihydrochloride	Sigma-Aldrich	Cat# D9542; CAS: 28718-90-3
Spectral DAPI	Akoya Biosciences	Cat# FP1490
TRIzol	Thermo Fischer Scientific	Cat# 15596026
Formalin solution, neutral buffered, 10%	Sigma-Aldrich	Cat# HT5012-1CS
Streptavidin agarose	Sigma-Aldrich	Cat# 69203
Trypsin Gold, Mass Spectrometry Grade	Promega	Cat# V5280
Water, LC-MS Grade	Thermo Fischer Scientific	Cat# 047146.K2
Methylcellulose	Sigma-Aldrich	Cat# M0512; CAS: 9004-67-5
Crystal violet	Sigma-Aldrich	Cat# C6158; CAS: 548-62-9
H&E staining solution	Vector Laboratories	Cat# H-3502
Bovine serum albumin (BSA)	Sigma-Aldrich	Cat# A2153; CAS: 9048-46-8
SuperSignal™ West Dura Extended Duration Substrate	Thermo Fisher Scientific	Cat# 34075
TSA-conjugated opal fluorophore Opal 620 Reagent Pack	Akoya Biosciences	Cat# FP1495001KT
TSA-conjugated opal fluorophore Opal 690 Reagent Pack	Akoya Biosciences	Cat# FP1497001KT
TSA-conjugated opal fluorophore Opal 650 Reagent Pack	Akoya Biosciences	Cat# FP1496001KT
TSA-conjugated opal fluorophore Opal 520 Reagent Pack	Akoya Biosciences	Cat# FP1487001KT
TSA-conjugated opal fluorophore Opal 540 Reagent Pack	Akoya Biosciences	Cat# FP1494001KT
TSA-conjugated opal fluorophore Opal 570 Reagent Pack	Akoya Biosciences	Cat# FP1488001KT
TSA-conjugated opal fluorophore Opal 480 Reagent Pack	Akoya Biosciences	Cat# FP1500001KT
TSA-conjugated opal fluorophore Opal 780 Reagent Pack	Akoya Biosciences	Cat# FP1501001KT
Critical commercial assays		
SensiFast cDNA synthesis kit	Meridian Bioscience	Cat# BIO-65054
SsoAdvanced Universal SYBR Green Supermix	Bio-Rad Laboratories	Cat# 1725271
One-Step RT-ddPCR Advanced Kit for Probes	Bio-Rad Laboratories	Cat# 1864021
SARS-CoV-2 Droplet Digital PCR Kit	Bio-Rad Laboratories	Cat# 12013743
Deposited data		
Targeting peptidyl-arginine deiminase 4 suppresses SARS-CoV-2 replication and modulates the inflammatory response	This paper; PRIDE data	PRIDE: PXD072601; https://www.ebi.ac.uk/pride/archive/projects/PXD072601

(*Continued on next page*)

Continued

REAGENT or RESOURCE	SOURCE	IDENTIFIER
Experimental models: Cell lines		
Vero-E6 cells	ATCC	Cat# CRL-1586; RRID:CVCL_0574
VERO-E6 TMPRSS2	kindly provided by John Hiscott, Pasteur Institute Rome	RRID:CVCL_YQ49
Calu3 cells	ATCC	Cat# HTB-55; RRID:CVCL_0609
Huh7.5 cells	kindly provided by Paola Cappello, University of Turin	RRID:CVCL_7927
Experimental models: Organisms/strains		
Transgenic B6.Cg-Tg (K18-hACE2)2Prlmn/J mice	The Jackson Laboratory	RRID:IMSR_JAX:034860
Oligonucleotides		
See Table S5		N/A
Software and algorithms		
Image Lab software (version 4.6.9)	Bio-Rad Laboratories	http://www.bio-rad.com/en-us/sku/1709690-image-lab-software; RRID:SCR_014210
Gen5	Agilent BioTek	RRID:SCR_017317
inForm Image Analysis software (version 2.6.2)	Akoya Biosciences	https://www.akoyabio.com/phenoimager/inform-tissue-finder; RRID:SCR_019155
MetaboAnalyst (version 5.0)	web platform	https://www.metaboanalyst.ca/; RRID:SCR_015539
Thermo Xcalibur (version 2.1)	Thermo Fischer Scientific	http://chemistry.unt.edu/~verbeck/LIMS/Manuals/XCAL_Quant.pdf; RRID:SCR_014593
Proteome Discoverer (version 2.1.1.21)	Thermo Fischer Scientific	https://www.thermofisher.com/order/catalog/product/IQLAAEGABSFAKJMAUH; RRID:SCR_014477
Mascot (version 2.6.2)	Matrix Science	http://www.matrixscience.com/server.html; RRID:SCR_014322
Scaffold Q + S (version Scaffold_5.3.0)	Proteome Software Inc.	RRID:SCR_014321
Protein Prophet algorithm	web platform	http://proteinprophet.sourceforge.net; RRID:SCR_000286
GraphPad Prism version 9.00 for Windows	GraphPad, Software, La Jolla, California, USA	www.graphpad.com; RRID:SCR_022798
Other		
Victor ×3 Multimode Microplate Reader	Perkin Elmer	Cat# 1420-050; RRID:SCR_027786
NanoDrop One Spectrophotometer	Thermo Fisher Scientific	Cat# ND-ONE-W; RRID:SCR_023005
CFX96 Touch Real-Time PCR Detection System	Bio-Rad Laboratories	Cat# CFX96 Touch; RRID:SCR_018064
QX200 Droplet Digital PCR System	Bio-Rad Laboratories	Cat# 1864001; RRID:SCR_019707
Cytation 5 Cell Imaging Multi-Mode Reader	Agilent BioTek	RRID:SCR_019732
ChemiDoc MP Imaging System	Bio-Rad Laboratories	Cat# 12003153; RRID:SCR_019037
gentleMACS Octo Dissociator with Heaters	Miltenyi Biotec	Cat# 130-096-427; RRID:SCR_020271
BOND RX automated immunostainer	Leica Biosystems	Cat# HIS2328; RRID:SCR_025548
Mantra Quantitative Pathology Workstation (version 2.6)	Akoya Biosciences	https://www.akoyabio.com/phenoimager/instruments/mantra-2
Vanquish Duo UHPLC System	Thermo Fisher Scientific	https://www.thermofisher.com/it/en/home/industrial/chromatography/liquid-chromatography-lc/hplc-uhplc-systems/vanquish-duo-uhplc-dual-lc-system.html

(*Continued on next page*)

Continued

REAGENT or RESOURCE	SOURCE	IDENTIFIER
Q-Exactive Plus UHMR Hybrid Quadrupole Orbitrap Mass Spectrometer	Thermo Fischer Scientific	Cat# 04331L; RRID:SCR_020556
Luna Omega 5 μm Polar C18 100 Å, LC 150 × 2.1 mm column	Phenomenex	Cat# 00F-4754-AN
SecurityGuard Cartridges, C18 4 × 3.0 mm	Phenomenex	Cat# AJ0-4287
LTQ-Orbitrap Discovery Mass Spectrometer	Thermo Fisher Scientific	Cat# 386859; RRID:SCR_020551
Easy-nLC HPLC	Thermo Fisher Scientific	Cat# LC140; RRID:SCR_026978
EnVision FLEX peroxidase-blocking reagent	Agilent	Cat# S2023
EnVision FLEX DAB	Agilent	Cat# GV82511-2
EnVision FLEX substrate buffer	Agilent	Cat# K3467
Immobilon-P PVDF membranes	Sigma-Aldrich	Cat# IPVH00010

EXPERIMENTAL MODEL AND STUDY PARTICIPANT DETAILS

Cell lines and viruses

African green monkey kidney Vero-E6 cells (ATCC-1586), VERO-E6 TMPRSS2 cells (kindly provided by John Hiscott, Pasteur Institute Rome), Calu3 cells (ATCC- HTB-55), and Huh7.5 (kindly provided by Paola Cappello, University of Turin) cells were propagated in Dulbecco's Modified Eagle Medium (DMEM high glucose; Sigma-Aldrich) supplemented with 1% (v/v) penicillin/streptomycin solution (Euroclone) and 10% (v/v) heat-inactivated fetal bovine serum (FBS; Sigma-Aldrich).

SARS-CoV-2 strains were isolated from positive nasal-pharyngeal swabs. The isolated SARS-CoV-2 strains belongs to the 2020B.1 lineage (SARS-CoV-2/human/ITA/Milan-UNIMI-1/2020, GISAID EPI_ISL_ 584051), Delta B.1.617.2 (GISAID EPI_ISL_6602889), Omicron B.1.1.529 (GISAID EPI_ISL_10898045), and XEc XBB.1.5/BA.2.86 (GISAID EPI_ISL_19468204). The 2020B.1 lineage, which carries the characteristic spike mutation D614G, represents the predominant European lineage originating from the early-2020 Northern Italian outbreak. The Delta and Omicron strains belong to parental lineages categorized as ''variants of concern'' (VOCs) due to their epidemiological relevance [https://www.ecdc.europa.eu/en/covid-19/variants-concern].

The replication-competent vesicular stomatitis virus rVSV-eGFP-SARS-CoV-2-SΔ21 was a kind gift from Sean P.J. Whelan (Washington University School of Medicine, USA).[52] The Spike gene used is based on the SARS-CoV-2 strain circulating in Europe in early 2020, closely related to lineage B.1.

For the *in vivo* experiments, we employed the SARS-CoV-2 Delta isolate (hCoV-19/Netherlands/NH-RIVM-27142/2021_P2) obtained from the European Virus Archive goes Global (EVAg) platform. Viral stocks were prepared by propagation in Vero E6 cells in DMEM supplemented with 2% FBS.

All experiments involving live SARS-CoV-2 were performed in accordance with the Italian Ministry of Health guidelines for BSL-3 containment procedures in the approved laboratories at the Molecular Medicine Department of the University of Padova.

Animal studies

In vivo studies were conducted using B6.Cg-Tg(K18-hACE2)2Prlmn/J (K18-hACE2) transgenic mice, a well-established model for SARS-CoV-2 infection.[71] Transgenic mice were purchased from The Jackson Laboratory, and housed and bred at the Specific Pathogen-Free animal facility of IOV-IRCCS. All procedures were approved by the Institutional Animal Care and Use Committee (IACUC) and conducted in certified BSL-3 containment laboratories at the University of Padova. Before the experiment, six-to 8-week-old K18-hACE2 mice were acclimatized within the BSL-3 facility for 72 h.

In the first experiment, mice were randomly distributed in four groups (n = 6 each) and intranasally inoculated with either 10 μL of phosphate buffer saline (PBS) (n = 6, mock-infected), or 10 μL of 1×10^5 PFU SARS-CoV-2 Delta strain (n = 12, SARS-CoV-2 infected). Throughout the experimental period, body weight and physiological conditions were monitored daily until euthanasia at 4 or 6 days post-infection (dpi). At 4 dpi, organs were collected and homogenized (Miltenyi, gentleMACS Octo Dissociator with Heaters) with TRIzol (Thermo Fischer Scientific) for RNA extraction. At 6 dpi, the right lobe of the lung and the right hemisphere of the brain were fixed in 10% buffered formalin for histopathology evaluation (multiplex immunofluorescence), while the left lobe and the left hemisphere were homogenized with RIPA buffer for protein extraction.

In the second experiment, mice were pre-treated one day prior to infection (pre-treatment), with BB-Cl-amidine (1 mg/kg), GSK199 (30 mg/kg), or vehicle (PBS 10% DMSO) via i.p. injection. Treatments were administered daily for 5 days. On day 0, mice were intranasally infected with 10 μL of SARS-CoV-2 Delta strain at 1×10^5 PFU. Body weight and physiological conditions were conducted until euthanasia at 4 dpi, when oropharyngeal swabs, lungs and brains were collected. The lungs and brains of four animals per group

were fixed in 10% buffered formalin (Sigma-Aldrich) for histopathological evaluation, while whole lungs and brains of six animals per group were homogenized (Miltenyi, gentleMACS Octo Dissociator with Heaters) with TRIzol (Thermo Fischer Scientific) for RNA and protein extraction following the manufacture's instruction.

All procedures involving the animals and their care adhered to institutional guidelines that comply with national and international laws and policies (D.L. 26/2014 and subsequent implementing circulars). The experimental protocol (Authorization No. 355/2021-PR) received approval from the Italian Ministry of Health.

METHOD DETAILS

Reagents and treatments

The PAD inhibitors Cl-A, BB-Cl, and GSK199 were purchased from Cayman Chemical. All the compounds were solubilized in DMSO (Sigma-Aldrich) according to the manufacturer's instructions. Immediately before use, the inhibitors were diluted in the culture medium to the working concentrations.

Cell viability assay

Cells were plated at 70% confluence in 96-well plates. After 24 h, cells were treated with different PAD inhibitors at the indicated concentrations or with an equal volume of the vehicle alone (DMSO). After 72 h, cell viability was determined by 3-(4,5-dimethylthiazol-2-yl)-2,5-diphenyltetrazolium bromide assay (MTT). Briefly, MTT solution (final concentration 500 μg/mL; Sigma-Aldrich) was added to the cell medium, and cells were incubated in the dark at 37°C in a CO_2 incubator for 2 h. The medium was removed, and the resulting formazan crystals formed by the cells were dissolved using 50 μL of DMSO. The absorbance was measured at 570 nm with a reference wavelength of 630 nm using a Victor ×3 Multilabel Plate Reader (PerkinElmer, Waltham, MA, USA; Wallac 1420 Workstation software).

In vitro antiviral assay

Cells were cultured in 24-well plates for one day. One h before infection, cells were pre-treated with PAD inhibitors or DMSO at the indicated concentrations. Subsequently, cells were infected with SARS-CoV-2 strains at the specified multiplicity of infection (MOI). Following virus adsorption (2 h at 37°C) and viral inoculum removal, new medium with fresh PAD inhibitors or DMSO alone was added to the plates and kept until sample harvesting at the indicated time points. The extent of SARS-CoV-2 replication was assessed by titrating the infectivity of supernatants using quantitative real-time PCR (qRT-PCR) and/or plaque assay conducted as described in the following paragraphs.

Quantitative real-time qRT-PCR (viral load)

Absolute quantification of SARS-CoV-2 copy numbers in cell supernatants was performed using specific qRT-PCR targeting the N1 gene, as described by Signorini et al.[72]

Plaque assay

Vero-E6 cells were plated the day before in a 6-well plate in complete medium (7.5×10^5/well). Briefly, after 2 h of inoculation with supernatants (500 μL/well), the inocula were removed, and the cells were overlaid with a 0.3% agarose gel dissolved in complete medium. Plates were then incubated at 37°C with 5% CO_2 for 48/72 h. Cells were then fixed with 4% formaldehyde, and after agarose removal, stained with 0.5% methylene blue. Plaques were counted, and the results were expressed as plaque-forming units per milliliter (PFU/mL).

RNA isolation and comparative qRT-PCR

Total RNA was extracted from cell and tissue samples using the TRI Reagent solution (Sigma-Aldrich) and quantified with a NanoDrop Spectrophotometer (Thermo Fischer Scientific). One μg of total RNA was reverse transcribed using the SensiFast cDNA synthesis kit (Meridian Bioscience) according to the manufacturer's instructions. Comparison of mRNA expression between treated and untreated samples was performed by SYBR green-based real time qRT-PCR with a Bio-Rad CFX96 apparatus (Bio-Rad Laboratories) using the primers indicated in Table S5.

The reaction conditions were as follows: 2 min at 95°C, followed by 40 cycles of 5 s at 95°C and 1 min at 60°C.

Droplet Digital PCR (ddPCR)

SARS-CoV-2 genomic RNA was quantified using the QX200 Droplet Digital PCR System (ddPCR, Bio-Rad Laboratories). One-Step RT-ddPCR Advanced Kit for Probes (Bio-Rad Laboratories) and the SARS-CoV-2 Droplet Digital PCR Kit (Bio-Rad Laboratories) were used following the manufacturer's instructions. SARS-CoV-2 quantification was expressed as a copy number/μg of total RNA.

Western blot analysis

Whole-cell protein extracts were prepared with RIPA buffer, quantified according to the Bradford method, and subjected to immunoblotting. Briefly, equal amounts of cell extracts were separated by SDS-PAGE and transferred to Immobilon-P membranes (Merck

Millipore). These were blocked in Tris-buffered saline (TBS) solution containing 0.05% Tween 20 and 5% milk and then incubated overnight at 4°C with appropriate primary antibodies: anti-CCP (Biorbyt, orb10262), anti-PAD2 (Proteintech, 12110-1-AP), anti-PAD4 (Proteintech,17373-1-AP), anti-actin (Sigma-Aldrich, A2066), anti-Nucleoprotein(N)_SARS-CoV-2 (GeneTex, 3851), anti-Spike(S)_SARS-CoV-2 (GeneTex, 1A9). Membranes were then washed and incubated for 2 h at room temperature with HRP-conjugated secondary antibodies (ECL anti-rabbit/mouse IgG, Cytiva). Proteins were visualized using the Bio-Rad ChemiDoc Imaging System and an enhanced chemiluminescence detection kit (SuperSignal West Dura Extended Duration Substrate, Thermo Fisher Scientific). Band densitometry was performed using Image Lab software (version 4.6.9; Bio-Rad Laboratories).

Detection of citrullination with rhodamine-phenylglyoxal (Rh-PG)

Equal amounts of protein were diluted with 80% trichloroacetic acid and incubated with Rh-PG (Cayman Chemical) at the final concentration 0.1 mM for 30 min. The reaction was quenched with 100 mM L-citrulline (Cayman Chemical), then centrifuged at 21100 × g for 10 min, washed with ice-cold acetone (Sigma-Aldrich), and resuspended in 2× SDS loading dye for gel electrophoresis. Gels were imaged (excitation = 532 nm, emission = 580 nm) using a Bio-Rad Chemidoc Imaging System (Bio-Rad Laboratories), then stained with brilliant blue G-colloidal solution (Sigma-Aldrich).

Neutralization assay

VERO E6 and VERO E6-TMPRSS2 were treated with GSK199 (20 μM) or BB-Cl (5 μM). After 1h of pretreatment, the medium was replaced with fresh medium lacking PAD inhibitors but containing rVSV-SARS-CoV-2-SΔ21 at an MOI of 0.05. Cells were incubated at 37 °C for 24 h in 96-well plates and then fixed in 4% formaldehyde (Sigma-Aldrich) containing DAPI (Sigma-Aldrich) for 15 min on ice. Images were acquired using Cytation 5 (Agilent BioTek) in both DAPI and GFP channels to visualize nuclei and infected cells (eGFP-positive cells). Images were segmented using the following building blocks: find nuclei, find cytoplasm, calculate GFP intensity, and select population (GFP^+ cells), and were further processed to calculate the ID50—the reciprocal dilution inhibiting 50% of the infection—using the Gen5 software (Agilent).

SARS-CoV-2 recovery from nasopharyngeal swabs and titration

Immediately upon collection, the swabs were submerged in FBS-free high-glucose DMEM (Sigma-Aldrich) and refrigerated. The medium was then rapidly employed to infect Vero E6 cells (9×10^4 cells/well in a 24-well plate) for 1 h. The infectious medium was then replaced with fresh DMEM containing 10% FBS, and supernatants were collected 48 h post-infection for titration. Briefly, Vero E6 cells were seeded in 24-well plates at a concentration of 9×10^4 cells per well. The following day, serial dilutions of viral stocks with known titers (infection-positive control) or test supernatants were prepared in serum-free DMEM. After 1-h incubation at 37°C, the overlay media was added to the inoculum, resulting in a final concentration of 2% (v/v) FBS in DMEM and 0.6% (v/v) methylcellulose (Sigma-Aldrich). Subsequently, the samples were incubated at 37 °C for 48 h and fixed using 5% formaldehyde in PBS (Sigma-Aldrich). The plaques were then visualized using a solution of crystal violet (0.5 g of crystal violet powder dissolved in 400 mL of distilled water and 100 mL of methanol (Sigma-Aldrich). Plaques were counted, and results were expressed as PFU/mL.

Histology and immunohistochemistry

Four-μm lung and brain sections were examined after H&E staining by a veterinary pathologist and an independent board-certified veterinary pathologist. Histological features were evaluated as the percentage of tissue involvement and blindly scored as follows: 0, no tissue involvement (no findings); 1, up to 25% of affected tissue (mild); 2, up to 50% of involved tissue (moderate); 3, up to 75% (severe); 4, up to 100% (massive). Finally, a total score per animal was obtained by combining cumulative scores of lesion types or anatomical compartments.

For SARS-CoV-2 antigen detection, slides were incubated with blocking reagent [5% bovine serum albumin (BSA) for 20 min, at RT] followed by exposure to a rabbit polyclonal antibody against SARS-CoV-2 N protein (1:300 in PBS, overnight, RT). Endogenous peroxidases were blocked using EnVision FLEX peroxidase-blocking reagent (3 min, RT; Agilent). A goat anti-rabbit IgG (H + L) secondary antibody conjugated to HRP (1:500 for 60 min, at RT) was then applied, followed by chromogen detection using EnVision FLEX DAB + chromogen (1 drop/mL of substrate buffer; Agilent) and EnVision FLEX substrate buffer (Agilent). Tissues were examined and scored post-examination in blind by a board-certified experimental pathologist.

Multiplex immunofluorescence

Tyramide signal amplification (TSA)-based opal staining (Akoya Biosciences) was used for mIF staining on a Leica BOND RX automated immunostainer (Leica Biosystems), as previously described.[73] Briefly, 4 μm-thick FFPE tissue sections were deparaffinized by baking O/N at 56 °C, soaking in BOND Dewax Solution at 72 °C, and then rehydrating in ethanol. Heat-induced epitope retrieval (HIER) pretreatments were applied at 97 °C using BOND Epitope Retrieval (ER) solutions (ER1 or ER2, Leica Biosystems), depending on the primary antibody utilized. Tissue sections were blocked with normal goat serum (Vector Laboratories) for 10 min before applying each primary antibody. Prior to multiplex staining, a fluorescent singleplex assay was carried out for each biomarker to determine the optimal staining conditions and the appropriate sequence of primary antibody application. The following primary antibodies were sequentially applied to the slides: SARS-CoV-1/2 Spike Protein (clone 2B3E5, Cell Signaling), mouse anti-mouse β-tubulin IV (clone T7941, Merck), rat anti-mouse F4/80 (clone CI:A3-1, Bio-Rad Laboratories), rabbit anti-mouse PAD2 (polyclonal,

Proteintech), rabbit anti-mouse PAD4 (polyclonal, Proteintech), rabbit anti-mouse Ly6g (clone EPR22909-135, Abcam), rat anti-mouse CD3 (clone CD3-12, Abcam), and rabbit anti-mouse cytokeratin 8 (clone EP1628Y, Abcam). HRP-conjugated secondary antibodies (goat anti-rabbit and goat anti-rat, both purchased from Vector Laboratories) were incubated for 10 min as appropriate. TSA-conjugated opal fluorophores (Akoya Biosciences) were then added for 10 min, followed by washing with buffer after each step. Spectral DAPI (Akoya Biosciences) was used as nuclear counterstain, and slides were mounted in ProLong Diamond Anti-fade Mountant (Thermo Scientific). Multiplex-stained slides were imaged using the Mantra Quantitative Pathology Workstation (Akoya Biosciences) at 20× magnification. The inForm Image Analysis software (version 2.6.2, Akoya Biosciences) was used to unmix multispectral images. A selection of representative multispectral images was used to train the inForm software to create algorithms to apply in the batch analysis of all acquired multispectral images. phenoptrReports (add-ins for R Studio from Akoya Biosciences) was used to calculate cell density data, as the sum of the cells positive for a specific marker, divided by the area analyzed from the same tissue slide.

Liquid-liquid extraction of inhibitors from lung and brain homogenates

Stock DMSO solutions of both inhibitors (20 mM) were diluted in a 20 mL volumetric flask to prepare a 5 μM working solution containing both analytes using H_2O LC-MS grade (Thermo Fischer Scientific). Calibrator solutions ranging from 1 to 50 nM were prepared by diluting the working solution with H_2O LC-MS grade (Thermo Fischer Scientific). To create a matrix-matched calibration curve and mimic analyte loss during liquid-liquid extraction, calibrators were spiked with tissue homogenate blanks and subjected to the same extraction procedure as that employed for the study samples.

The liquid-liquid extraction protocol was as follows: 50 μL of sample or blank matrix aliquot were mixed with 50 μL calibrator or H_2O neat solvent for study samples, 50 μL of 10 mM NaOH, 5 μL of saturated NaCl solution, 20 μL of 5.5% w/v $ZnSO_4$ solution, and 400 μL of ethyl acetate (organic phase). The biphasic system was stirred for 10 min to maximize analyte transfer to the organic phase. The emulsion was separated using a benchtop centrifuge at 13,000 rpm for 5 min. A 200 μL aliquot of the organic phase was transferred to microtubes, and the extraction process was repeated three times to collect a total of 600 μL of organic phase per sample. Extracts were dried using an evaporator centrifuge set to 40°C under vacuum for 1 h. Dried extracts were reconstituted in 50 μL of ACN:H_2O (1:1) and analyzed through LC-MS/MS. This procedure was optimized to enhance separation, considering the basic groups in both GSK199 and BB-Cl. During the analytical run, samples were stored in an autosampler of the Vanquish Duo UHPLC system at 15°C.

Inhibitor concentrations were converted from nM to μg of inhibitor per g of organ. Data processing was conducted using the MetaboAnalyst web platform, with all data normalized via logarithmic transformation to achieve a normal distribution. Subsequent statistical analysis involved heatmaps to depict the abundance of the inhibitor across study samples.

LC-HRMS analyses

A Q-Exactive Plus UHMR Hybrid Quadrupole Orbitrap Mass Spectrometer coupled with a Vanquish Duo UHPLC system (Waltham) was employed for LC-MS/MS analysis. Chromatographic separations were executed on a Luna Omega 5 μm Polar C18 100 Å, LC 150 × 2.1 mm column (maintained at 45°C) and protected by a C18 SecurityGuard (Phenomenex srl). Aliquots (10 μL) of homogenate extracts were injected and eluted using a mobile phase (flow rate 0.3 mL/min) consisting of A: H_2O 0.1% FA v/v; and B: ACN 0.1% FA v/v. The gradient elution profile was: 0.00–8.25 min [5–75% B], 8.25–9.25 min [75% B], 9.25–9.50 min [75-5% B], 9.50–12.5 min [5% B], for a total runtime of 12.5 min, including re-equilibration. The autosampler was maintained at 15°C. Successively, the eluate was introduced into the electrospray ion source, and MS data were acquired and processed using Xcalibur software. The operating conditions for the Orbitrap mass spectrometer were as follows: ESI ionization (±), spray voltage 3.50 kV, capillary temperature 300°C, sheath gas flow (N2) 45 L/min, sweep gas flow (N2) 1 L/min, auxiliary gas flow (N2) 10 L/min, auxiliary gas temperature 350°C, maximum spray current 100 μA, probe positioning settings: C, side-to-side position set to 0, micrometer set to 1.75. Data acquisition was performed in Full MS-SIM (+) within the scan range 100–1500 m/z, resolution 70,000, AGC target 3e6, maximum IT 200 ms; PRM (+) settings included resolution 35,000, AGC target 1e5, maximum IT 120 ms, loop count 1, MSX count 1, isolation window 4.0 m/z. Inclusion list parameters were set as follows: GSK199 [M + H+:433.23465 m/z], CE 28; BB-Cl [M + H+:460.18986 m/z], CE 28. Calibration curves were plotted using 1/x weighting linear regression via Xcalibur software.

Citrullinome analysis by mass spectrometry: Sample preparation

Sample preparation in technical triplicates followed the procedure outlined in Tilvawala et al.[31] Equal amounts of cell lysates from each experimental group (500 μg) were diluted in buffer (100 mM HEPES pH 7.6) to a final concentration of 1 μg/μL and incubated with 20% trichloroacetic acid (TCA) and 0.5 mM biotin-PG for 30 min at 37 °C. Labeled proteomes were precipitated on ice for 30 min. Samples were pelleted by centrifugation (21,100 × g, 15 min, 4 °C). Supernatants were discarded, and pellets were washed with 300 μL of cold acetone. After drying for 5 min, the pellets were resuspended in 1.2% SDS in PBS by bath sonication and heating. Samples were then transferred to 15 mL screw cap tubes and diluted in 1× PBS to a final SDS concentration of 0.2%. Streptavidin agarose slurry (Sigma Aldrich, 170 μL) was added, and samples were incubated O/N at 4 °C, followed by an additional 3 h at 25 °C. After discarding the flow through, the streptavidin beads were washed with 0.2% SDS in PBS (5 mL, 10 min, 25 °C), followed by three washes with 1× PBS (5 mL) and three washes with water (5 mL) to remove unbound proteins. The beads were then transferred to a screw cap microcentrifuge tube and heated in 1× PBS with 500 μL 6 M urea and 10 mM DTT (65 °C, 20 min). Bead-bound proteins

were alkylated with iodoacetamide (20 mM, 37 °C, 30 min). The beads were successively pelleted by centrifugation (1,400 × g for 3 min), and the supernatant was removed. Pellets were resuspended in a premixed solution of 2 M urea, 1 mM $CaCl_2$, and 2 μg Trypsin Gold (Promega) in PBS. These were shaken overnight at 37 °C. Supernatants were collected, and the beads were washed twice with water (50 μL), each time collecting the supernatant. The fractions were combined, acidified with formic acid (5% final concentration), and stored at −20 °C until use.

Mass spectrometry

Liquid chromatography-mass spectrometry/mass spectrometry (LC-MS/MS) analysis was performed with an LTQ-Orbitrap Discovery mass spectrometer (Thermo Fisher Scientific) coupled to an Easy-nLC HPLC (Thermo Fisher Scientific). Samples were pressure loaded onto a 250-μm fused-silica capillary hand packed with 4-cm Aqua C18 reverse phase resin (Phenomenex). Peptide separation was performed on a hand packed 100-μm fused-silica capillary column with a 5-μm tip packed with 10 cm Aqua C18 reverse phase resin (Phenomenex). Peptides were eluted using a 10-h gradient of 0–100% buffer B in buffer A (buffer A: 95% water, 5% acetonitrile, 0.1% formic acid; buffer B: 20% water, 80% acetonitrile, 0.1% formic acid). The flow rate through the column was set to ∼400 nL/min, and the spray voltage was set to 2.5 kV. One full MS scan (FTMS) was followed by 7 data-dependent MS2 scans (ITMS) of the nth most abundant ions. The mass spectrometry proteomics data have been deposited to the ProteomeXchange Consortium via the PRIDE[74] partner repository with the dataset identifier PXD072601.

Database search

Raw data were processed using Proteome Discoverer (Thermo Fischer Scientific, version 2.1.1.21) and searched against Uniprot SARS-CoV-2 (downloaded 05/2024), Swiss-Prot human (downloaded 04/09/2019), and SwissProt murine (downloaded 07/2019) using Mascot (Matrix Science, version 2.6.2). The mass tolerance was 10 ppm for precursor and 0.05 Da for the fragment ions. Full tryptic cleavages were considered along with static modifications of carbamidomethylation (cysteine) and TMT labeling (peptide N-terminal and lysine), as well as dynamic modifications including acetylation (protein N-terminal), oxidation (methionine), and glutamine to pyroglutamate conversion (peptide N-terminal). Scaffold Q + S (version Scaffold_5.3.0, Proteome Software Inc.) was used to validate MS/MS based peptide and protein identifications and quantify label-based quantitation (TMT). Peptide identifications were accepted at greater than 91.0% probability using the Peptide Prophet algorithm[75] with Scaffold delta-mass correction. Protein identifications were accepted at greater than 90.0% probability and required at least two identified peptides. Protein probabilities were assigned using the Protein Prophet algorithm.[76] Proteins with indistinguishable peptides were grouped according to the principles of parsimony. Proteins sharing significant peptide evidence were clustered together. Channels were corrected in all samples using the algorithm described in i-Tracker.[77] Normalization was performed iteratively on intensities as previously described.[78] Medians were used for averaging. Spectra data were log-transformed, pruned of those matched to multiple proteins, and weighted using an adaptive intensity weighting algorithm. Differentially expressed proteins were determined by applying Mann-Whitney Test with Benjamini-Hochberg correction.

Ethics approval statement

All experiments involving active SARS-CoV-2 viral particles were performed in a Biosafety Level-3 (BSL-3) laboratory at the ParVirLab, University of Milan in compliance with institutional and national biosafety regulations. Nasal pharyngeal swabs were collected upon approval from the Local Ethics Committee, after obtaining informed consent. This study was conducted under protocol No. 456_2020 approved by The Fondazione Ca' Granda, Ospedale Maggiore, Milano, Italy, in May 2020.

QUANTIFICATION AND STATISTICAL ANALYSIS

Quantification and statistical analyses were performed using GraphPad Prism software (version 10.6.1). The statistical tests applied, the number of independent biological replicates (n), and the definition of significance thressholds (asterisks) are indicated in the corresponding figure legends. Data are presented as mean ± SEM unless otherwise specified. Normality was not assumed for *in vivo* datasets, and non-parametric tests were applied where appropriate. Comparisons between two groups were performed using unpaired two-tailed t-tests or non-parametric t-tests, as specified in the figure legends. For experiments involving multiple conditions, one-way ANOVA followed by Bonferroni's post hoc test was used. For proteomic analyses, including volcano plots, statistical processing was performed within the mass spectrometry workflow as detailed in the STAR Methods. Briefly, intensity values were log-transformed and normalized, and differential citrullination was assessed using a Mann–Whitney test with Benjamini–Hochberg correction for multiple comparisons. Individual biological replicate values and the corresponding statistical analyses for each figure panel are provided in the Data S1 file, that includes the unedited and uncropped western blot images with molecular weight markers indicated.